공학박사 학위논문

Functional production, analyses, and applications of human taste receptors and photoreceptors

인간 미각 수용체 및 광수용체의 기능적 생산, 분석 및 응용

2023년 2월

서울대학교 대학원

공과대학 협동과정 바이오엔지니어링 전공

차 연 경

Functional production, analyses, and applications of human taste receptors and photoreceptors

지도 교수 박 태 현

이 논문을 공학박사 학위논문으로 제출함

2023년 2월

서울대학교 대학원

공과대학 협동과정 바이오엔지니어링 전공

차 연 경

차연경의 공학박사 학위논문을 인준함

2023년 2월

위 원 장 황 석 연 (인)

부위원장 박 태 현 (인)

위 원 김 지 현 (인)

위 원 송 현 석 (인)

위 원 이 승 환 (인)

Abstract

Functional production, analyses, and applications of human taste receptors and photoreceptors

Yeon Kyung Cha

Interdisciplinary Program in Bioengineering

The Graduate School

Seoul National University

G protein-coupled receptors (GPCRs) are the largest transmembrane protein family, mediating the majority of cellular responses such as vision, taste, olfaction, neurotransmitters, and hormones. Measuring the activity and function of GPCR is critical in food, environmental, and biomedical applications. Therefore, producing and engineering functional GPCRs are important in developing tools for GPCR research and practical applications. Humans have five senses: sight, taste, smell, hearing, and touch. Among the five senses, the senses of vision, taste, and smell involve GPCR signaling. Class A GPCRs include photoreceptors and olfactory receptors responsible for vision and smell. Class C GPCRs include taste receptors for sweet and umami taste, often known as “palatable” taste.

In these theses, various approaches to engineer and produce human taste receptors and visual photoreceptors were performed. For utilizing human sweet and umami taste receptors, a primary ligand binding domain of the receptor was mass-produced from *E. coli* as an alternative strategy to using a

whole receptor, which is difficult to overexpress in *E. coli*. These were analyzed independently with tryptophan fluorescence assay and combined with conducting nanomaterials to evaluate sweet and umami taste in a practical manner. Human photoreceptor NDs produced from *E. coli* and photoreceptor-expressing virus produced from mammalian cells were analyzed to better understand the physiological and biochemical mechanisms in human photoreceptors and to further apply this knowledge to develop vision restoration technologies.

First, a primary ligand-binding domain of a human sweet and umami taste receptor, the T1R2 VFT and T1R1 VFT, were functionally produced from *E. coli* as an alternative strategy to using a whole receptor. The functions were analyzed by tryptophan fluorescence assay using the representative taste molecule, sucrose, and MSG, respectively. Functionally refolded VFTs have been validated for use as a biomaterial for detecting sweet and umami substances.

Second, the ligand-binding domain of the human sweet taste receptor was used to evaluate sweet taste substances in a practical manner. Tryptophan fluorescence analysis, a relatively simple approach for measuring sweet taste using T1R2 VFT of human sweet receptors, was used to assess the efficacy of sweet taste compounds. The tryptophan assay results were expressed as relative sweetness to provide a quick and simple way to interpret ligand binding at the receptor level. Furthermore, a T1R2 VFT was immobilized on the floating electrode of a CNT-FET to develop a protein-based biosensor for the practical detection of sweet compounds.

Third, the ligand-binding domain of the human umami taste receptor was used to evaluate umami taste substances and their synergistic effects using tryptophan

fluorescence assays. Furthermore, a T1R1 VFT was hybridized with floating electrode-based CNT-FET and combined with a conductive polymer hydrogel. The hydrogel-mediated CNT-FET with T1R1 VFT was anticipated to be a useful tool for detecting umami compounds in foods, as well as a significant application in the food sector and fundamental research.

Lastly, the photoreceptors were either produced in *E. coli* and mammalian cells, and they were used in a variety of experiments and applications. Photoreceptor NDs produced from *E. coli* were used for measuring the optical properties of their potential optical applications, such as optical switching. Photoreceptor-expressing virus produced from mammalian cells was used for developing *in vitro* model of a neural circuit for the eye to the brain.

In this study, various approaches to engineering and producing human taste receptors and visual photoreceptors were used. Various analyses and applications using engineered human sensory receptors were also investigated for a better understanding of human taste and vision and future food, environmental, and biomedical applications.

Keywords: G protein-coupled receptor (GPCR), human sweet taste receptor, human umami taste receptor, human photoreceptor, ligand binding domain, nanobiosensor, nanodisc

Student Number: 2017-29229

Table of Contents

List of Figures

List of Tables

List of Abbreviations

cAMP: cyclic adenosine monophosphate

CNT: carbon nanotube

DLS: dynamic light scattering

DMEM: Dulbecco's Modified Eagles Medium

E. coli: *Escherichia coli*

EDTA: dthylenediaminetetraacetic acid

FBS: fetal bovine serum

FE-SEM: field-emission scanning electron microscopy

FET: field-effect transistor

GPCRs: G protein-coupled receptors

GFP: green fluorescent protein

HEK-293 cell: human embryonic kidney 293 cell

IP3: inositol (1, 4, 5) trisphosphate

IPTG: Isopropyl β-D-1-thiogalactopyranoside

LOD: limit of detection

LBD: ligand binding domain

LW: long wave sensitive opsin

MSP: membrane scaffold protein

MW: medium wave sensitive opsin

M: mole

ND: nanodisc

PBS: phosphate-buffered saline

Photoreceptor: photoreceptor protein, opsin

Rho: rhodopsin

RFP: red fluorescent protein

SW: short wave sensitive opsin

SDS: sodium dodecyl sulfate

SDS-PAGE: sodium dodecyl sulfate-polyacrylamide gel electrophoresis

SEC: size exclusion chromatography

VFT: venus flytrap domain

V: gate voltage

Chapter 1

Research background and objective

Research background and objective

Animals, including humans, can discern nutrition through the sensation of sweet and umami tastes. Sweet and umami tastes are perceived as 'palatable' taste by humans through taste receptor type 1 (T1R) family. Sweet and umami taste receptors are heterodimeric class C GPCRs in the T1R family; T1R2/T1R3 is a sweet taste receptor and T1R1/T1R3 is an umami taste receptor. Class C GPCRs are composed of three subunits: extracellular ligand-binding domain (Venus flytrap (VFT)), cysteine-rich domain (CRD), and transmembrane domain (TMD). T1R2 VFT and T1R1 VFT are known to play a significant role in ligand binding. The primary step in taste recognition is the binding of taste molecules to a taste receptor, which then activates the receptors for subsequent reactions. Therefore, researchers have taken a keen interest in taste receptors, not only in understanding the structure-function relationship but also utilizing taste receptors to detect taste compounds for food, beverage, and pharmaceutical applications.

Rod cells and cone cells are the two types of light-sensitive cells existing in the human photoreceptor cell layer. The outer segment of the photoreceptor cells consists of several discs, and light-sensitive photoreceptor opsins exist in the membrane of the disc. These photoreceptors, which are rhodopsin and cone opsin, share a similar mechanism, and in vivo, photoreceptor protein is coupled to 11-*cis*-retinal, a vitamin A derivative, where it exhibits an inactive configuration. In the presence of light, the 11-*cis*-retinal molecule transforms into an all-*trans*-retinal and is freed from the photoreceptor. At the same time, the photoreceptor undergoes a structural conformational change that triggers off a chain of reactions that leads to signal transduction. There are four types of photoreceptors among these cells: rhodopsin (Rho) in rod cells that separates light from dark, and three types of cone

opsins (SW, MW, LW) in cone cells that identify colors. These four photoreceptors absorb light in various wavelengths.

GPCRs have been reported to be difficult to overexpress, solubilize and purify due to their complex structures and strong hydrophobicity, and it is difficult to obtain a sufficient amount of purified GPCRs for ligand binding studies. Although the bacterial expression system is known to be more efficient than the mammalian expression system in terms of high-level protein production, the sweet taste receptor, which has a heterodimeric, large, and complex structure, is difficult to be expressed.[1,2]

Proteins reconstituted using nanodisc (ND) are highly stable, compared to other reconstituted proteins.[3] In particular, ND technology is known to be suitable for restructuring G protein-coupled receptors. The ND consists of a receptor protein, a phospholipid bilayer, and a membrane scaffold protein (MSP), which encloses the receptor-phospholipid complex which acts as a belt. ND technology can mimic the structure of membrane proteins in nature.

In this chapter, four human photoreceptors were expressed and purified from *E. coli*.

In summary, the objectives of this study are:

1. Production of T1R2 VFT and T1R1 VFT, a primary ligand binding domain of human sweet and umami taste receptor, in *E. coli* system and functional characterization of refolded VFTs
2. Analysis of T1R2 VFT utilizing tryptophan fluorescence assay and development of bioelectronic tongue based on T1R2 VFT for evaluating sweet taste
3. Analysis of T1R1 VFT utilizing tryptophan fluorescence assay and

development of hydrogel-mediated CNT-FET based on T1R2 VFT for evaluating umami taste in fish extract samples

4. Production of human photoreceptors in both *E. coli* and mammalian cells using nanodisc technology and recombinant lentiviral systems
5. Photoreceptor NDs and photoreceptor-expressing viruses: analysis and applications in optical and medicinal applications

Chapter 2

Literature review

2.1 G protein-coupled receptors

GPCRs are known as the largest family of transmembrane proteins. It has seven transmembrane helices and mediates the majority of cellular responses regarding vision, taste, olfaction, neurotransmitters, and hormones.[4] GPCRs, when activated by specific stimuli, initiate a cascade of intracellular responses via interactions with their G-protein partners, which are comprised of three subunits: Gα, Gβγ and guanosine triphosphate (GTP).[5,6]

GPCRs are classified into several groups based on sequence conservation, functional similarity, and structural features.[5,7,8] Classes, A, B, and C are the most commonly studied GPCRs, which are rhodopsin-like, secretin-like, and metabotropic glutamate receptors. Although all GPCRs have structurally similar transmembrane domains, the ligand binding sites vary significantly within the GPCR superfamily. As a result, GPCR classification provides critical information for developing a production strategy and estimating functional activity.[9]

Measuring the GPCR activity and function is critical in food, environmental and biomedical applications. The existing functional assays require time-consuming, labor-intensive, and high-cost fluorescence assays involving whole cells expressing GPCRs.[10,11] As a result, developing tools for functional GPCR research is critical. Producing functioning GPCRs and integrating them with a conducting material to develop a biosensor platform will aid in the development of high-throughput assays for GPCR deorphanization and ligand screening.

2.2 Sensory transduction in taste and vision

Sweet and umami tastes are perceived as 'palatable' taste by a human through taste receptor type 1 (T1R) family. Sweet and umami taste receptors are heterodimeric class C GPCRs in the T1R family; T1R2/T1R3 is a sweet taste receptor and T1R1/T1R3 is umami taste receptor. Class C GPCRs are composed of three subunits: extracellular ligand-binding domain (Venus flytrap (VFT)), cysteine rich domain (CRD), and transmembrane domain (TMD).[12] The T1R2 VFT provides primary binding sites for majority of sugars and artificial sweeteners, whereas T1R1 VFT detects umami tastants and enhancers. Additionally, the T1R2 TMD enables for G-protein coupling and T1R3 CRD is known to be involved in binding of sweet proteins, monellin, and brazzein.[13-15]

Visual photoreceptors are classified as class A GPCRs, also known as the rhodopsin-like family, which has the most GPCR members.[7] Opsin is a class A GPCR with a short N-terminal extracellular domain, a transmembrane domain, and a short C-terminal intracellular domain. In class A GPCRs, orthosteric binding sites are found in the transmembrane helical bundle.[16]

2.2.1 Taste signal transduction

The T1R2/T1R3 receptor identifies a wide range of sweet compounds, including natural sugars, artificial sweeteners, amino acids, and proteins.[13,17,18] Gα-gustducin pathway is required for taste signal transduction. Sweet taste transduction occurs via two additional signaling pathways involving different secondary messengers, in addition to the G-gustducin pathway. The first involves cAMP, while the second involves IP3. [19,20] Sucrose or other sugars bind to TAS1R2 or TAS1R3

and recruit Gαs protein, resulting in increased cAMP levels and the influx of cations through ion channels. Then, cAMP activates protein kinase A, which causes TRC cell depolarization, resulting in calcium ion influx and releasing neurotransmitters. [21,22] Sweetener binding to the TAS1R2/TAS1R3 heterodimer, on the other hand, recruits G-gustducin proteins, which stimulate PLC2, which hydrolyzes phosphatidylinositol 4,5-bisphosphate (PIP2) to diacylglycerol (DAG) and IP3.[22]. IP3R3-induced Ca2+ release from ER stores activates TRPM5, resulting in action potential and releasing neurotransmitters.

The umami taste transduction mediated by T1R1/T1R3 is similar to those for sweet taste. [23] Both, α-transducin and α-gustducin are involved in umami taste signal transduction. Ligand binding to the T1R1/T1R3, releases Gβγ subunits to stimulate PLCβ2, which hydrolyzes PIP2 to DAG and IP3.[24] IP3 then activates IP3R3 which results in the release of calcium ions from intracellular compartments. Calcium ions activate TRPM5 and TRPM4 channels, leading to an influx of sodium ions, subsequent cell membrane depolarization, and finally release of neurotransmitters.

2.2.2 Visual phototransduction

Phototransduction is the process by which a photon of light captured by a molecule of visual pigment generates an electrical response in a photoreceptor cell. Visual photoreceptors are members of the superfamily of GPCRs whose natural ligand, the chromophore 11-*cis* retinal, is already covalently attached.[25] The 11-*cis* isomer acts as a powerful antagonist, and it is only when a photon of light isomerizes the chromophore to its all-*trans* form, which acts as a powerful agonist, that the visual pigment GPCR becomes active. Vision starts with the absorption of photons, and the photon-triggered isomerization of the retinal from the 11-*cis* to the

all-*trans* state, followed by conformational changes in the 7TM domain of rhodopsin to accommodate the binding of G proteins, leading to the downstream signal transduction, which is dominated by the kinetics of activation of the cGMP signaling pathway.[26]

2.3 GPCRs produced from heterologous expression system

2.3.1 GPCRs production in prokaryotic cells

The bacterial cell system has many advantages for producing recombinant proteins, including low cost, well-established molecular biological knowledge, homogeneity of the produced proteins, and short generation time. Furthermore, processes based on bacterial cell systems are easily optimized for large-scale production.[27,28] Because of these advantages, numerous attempts have been made to establish an optimal process to produce GPCRs using bacterial cell systems, especially Escherichia coli (*E. coli*). Among the different steps of the production process, expression is the initial step, and the quantities of GPCRs produced mostly depend on the expression level. However, it is difficult to overexpress membrane proteins including GPCRs in bacterial cells for various reasons. The expression of GPCRs in bacterial cell membranes is highly unpredictable, and the mechanism of insertion into the cell membrane is not well understood.[29] It has been accepted that eukaryotic membrane proteins are difficult to insert and express in prokaryotic cell membranes due to their different charge distribution on the cell surface and the mechanism of insertion.[30] In addition, the limited capacity of the bacterial cell membrane means that it cannot incorporate sufficient quantities of GPCRs. With more recent approaches, high-level expression of GPCRs has been achieved in an aggregated form as inclusion bodies. Expression of membrane protein in inclusion bodies reduces the toxicity during expression and simplifies the purification method. In this case, functional reconstitution is required after the solubilization of insoluble fractions and purification. To optimize the process, various conditions affecting the expression level, including the genotype of the host cell, the incubation time and temperature, and the induction conditions, need to be examined.[31-33]

2.3.2 GPCRs production in eukaryotic cells

As a eukaryotic cell system, insect cells perform posttranslational modifications, such as phosphorylation, fatty acid acylation, and glycosylation, and eukaryotic recombinant proteins produced using insect cells exhibit characteristics similar to those of their native forms.[34,35] For the production of GPCRs, insect cells offer correct folding in cell membranes with certain Gα subunits.[36] Along with these advantages, insect cells used as host cell systems have shown high efficiency for the expression of GPCRs. Several reports suggested that the expression levels of receptors were 25−600 times higher than those in mammalian cells, and the receptors exhibited the correct function for ligand binding.[37-39]

2.4 Nanobiosensors using natural receptors

Recently, nanobiosensors, which consist of biological recognition elements as a primary transducer, and nanomaterials, such as carbon nanotube (CNT), conducting polymer nanotube (CPNT), and graphene, as a secondary transducer for signal amplification, have been developed. The biological recognition elements allow a selective interaction with specific target molecules. The nanomaterials with outstanding electrical properties have enabled the development of novel or improved electrical sensing platforms with high sensitivity. Thus, the integration of biomaterials and nanomaterials facilitates the high sensitivity and selectivity of nanobiosensors. The various types of FET-based nanobiosensors using natural receptors as recognition elements for the bioelectronic nose and bioelectronic tongue are shown in **Figure 2.1**.

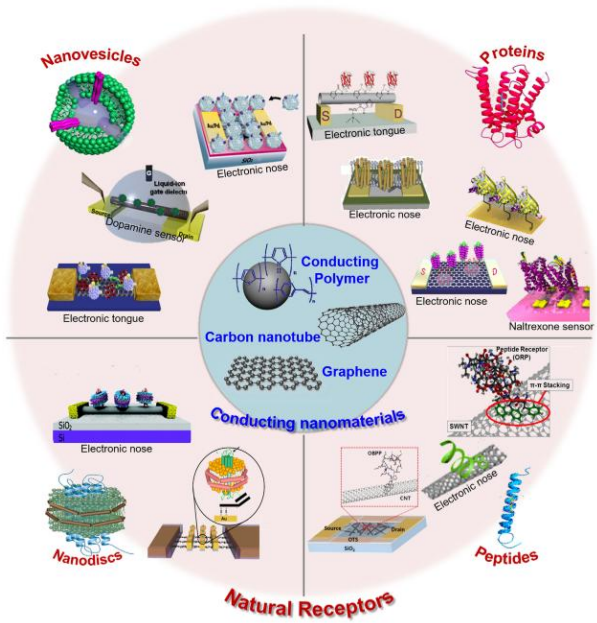

Figure 2.1 Various types of FET-based nanobiosensors using natural receptors

Kwon et al., Chem. Rev. 119, 36−93 (2019)

2.4.1 Protein-based biosensors

Natural receptor proteins are used in protein-based biosensors, which are made up of natural receptors produced by heterologous cell systems and secondary signal transducers. Secondary signal transducers detect the selective binding of natural receptors with ligands. In terms of stability, reusability, mass production, and ease of fabrication, natural receptor protein-based biosensors offer an advantage over cell-based biosensors. The bioelectronic nose is an example of a natural receptor protein-based biosensor. The human nose and mammalian olfactory system can discern between scents from different substances with single-carbon-atomic resolution, due to an olfactory that transmits signals to the brain, leading to smell identification via brain communication. The olfactory system's primary skill is to distinguish scents, even nonodorant gases. As a result, conventional electronic noses have been evaluated to mimic the human olfactory system, with numerous achievements in food, beverage, environmental monitoring, and illness diagnosis applications. Nonetheless, significant restrictions such as precise selection and ultrasensitivity must be overcome. An approach for immobilizing several types of olfactory and taste receptors on sensing platforms has also been developed.

2.4.2 Nanodisc-based biosensors

Human olfactory receptors embedded in detergent micelles or NDs have been used in nanobiosensors to reconstitute membrane receptor proteins.[40-42] NDs show remarkable reconstituted stability, comparable to other reconstituted proteins.[43] The ND is composed of phospholipids, which mimic the natural environment of the cell membrane, and MSP, which encircles the hydrophobic area of the phospholipid bilayer to ensure the receptor's stability. In the realm of nanobiosensors, the most

promising biomaterial is ND. However, E. coli lacks posttranslational modification processes for eukaryotic receptors, such as glycosylation and phosphorylation. E. coli is not suited for producing receptors that require post-translational modification. Membrane proteins reconstituted by detergents have limitations due to a lack of native membrane environment, such as denaturing the membrane proteins and reconstituted membrane protein stability.[44]

2.4.3 Nanovesicle-based biosensors

The signal pathway of nanovesicles produced from artificial cells expressing olfactory and taste receptors is considered to be similar to that of olfactory neurons and taste buds. [45,46] In HEK-293 cells expressing human olfactory receptors, the intracellular calcium ion concentration increased in response to odorant activation. It is assumed that the signal transduction of olfactory receptors produced in HEK-293 cells makes use of the cells' intrinsic components. Similarly, calcium ion influx was only observed in nanovesicles that integrated human olfactory and taste receptors through odorant binding. Calcium ion influx occurs via signal pathway cascade after certain ligands bind to receptors on the surface of nanovesicles, and is transferred to electrical signals via transducers such as CNT-FET. The advantage of utilizing nanovesicles over artificial cells is that they are more stable. This nanovesicle-based system mimics the human sensory pathway and exhibits olfaction and taste signal transduction, which is generated by ligand receptor contact, similar to artificial cells. GPCR-embedded nanovesicles exhibit a high storability and are less dependent on environmental factors. However, the limited reusability due to irreversible calcium influx should be taken into consideration in future research for practical nanobiosensors.[44]

2.4.4 Peptide-based biosensors

Peptides as recognition elements for CN-based sensor platforms should have various advantages over whole receptor proteins or nanovesicles, such as an easier synthesis procedure, higher stability, and an efficient Debye length for a FET-type transducer. Extensive structural research and computational modeling have enabled the prediction of binding sites and the identification of peptides that mimic natural receptor binding capabilities. Peptides derived from natural receptors have been used as recognition elements in biosensors coupled with a variety of signal transducers. Peptides are more suitable biomolecular structures for natural receptor-based FET systems than whole proteins because the sensing mechanism of FETs is dependent on the Debye length, which is the distance between the FET surface and charges on the analyte coupled to the FET. As a result, natural receptors in smaller forms have higher sensitivity and selectivity.[44]

Chapter 3

Experimental procedures

3.1 Gene cloning

3.1.1 Cloning of T1R2 VFT, T1R1 VFT and photoreceptor genes into *E. coli* expression vector

For cloning of T1R2 VFT or T1R1 VFT into *E. coli* expression vector, a signal peptide (1−20 amino acids)-deleted T1R2 or T1R1 VFT gene was amplified by polymerase chain reaction (PCR) with human genomic DNA as a template. A human cDNA, pCMV6-ENTRY-hTAS1R2 or hTAS1R1, was purchased from OriGene (USA). The amplified PCR product was cloned into a pENTR cloning vector using directional TOPO cloning, and then LR Clonase was used to clone it into pET-DEST42 expression vector (all from Invitrogen). For purification, the T1R2 VFT or T1R1 VFT gene was cloned into a pET-DEST 42 bacterial expression vector with the 6× His tag at the C-terminus.

In order to clone the photoreceptor SW or Rho genes into *E. coli* expression vector, the genes were amplified by a PCR using human SW and Rho cDNA clones as templates (available for purchase from OriGene Cat. No. RC222804, RC211328). Amplified PCR products were inserted into the pENTR cloning vector via directional TOPO cloning and transferred to the pET-DEST42 vector with LR Clonase (all from Invitrogen) for high-level bacterial expression and simple purification with C-terminal 6xHis tag.

3.1.2 Cloning of photoreceptor gene into mammalian expression vector

The photoreceptor genes in the pCMV6-entry vector were purchased from

OriGene (USA). These photoreceptor genes were cloned into pcDNA3 mammalian expression vectors (Invitrogen, USA). DNA sequencing was used to confirm their sequences (GenoTech, Korea). Additionally, Rho-EGFP and LW-DsRed in pcDNA3 vector were also constructed and confirmed by DNA sequencing.

3.1.3 Cloning of photoreceptor gene into lentiviral expression vector

The SW or Rho genes were amplified by PCR from with human genomic DNA as a template. The amplified Rho-tagged SW or Rho gene was inserted into the NheI and BamHI sites of the lentiviral vector pCDH-CMV-MCS-T2A-RFP-EF1-Puro. The sequence was confirmed by DNA sequencing.

3.2 Protein production from *E. coli*

3.2.1 Expression and purification of T1R2 VFT, T1R1 VFT and photoreceptors in *E. coli*

For production of T1R2 VFT or T1R1 VFT from *E. coli*, the cloned pET-DEST42 T1R2 VFT or pET-DEST42 T1R1 VFT was transformed into *E. coli* Rosetta (DE3) strain, and the transformed cell was cultured in a lysogeny broth media with ampicillin (50 μg/mL) at 37 °C. At the optical density (OD_{600}) value of 0.5, T1R2 VFT or T1R1 VFT gene expression was induced using 0.5 mM isopropyl β-D-thiogalactoside. Cells were incubated for 4 h and were harvested by centrifugation (7000g, 20 min, 4 °C). Cell pellet was resuspended in phosphate buffered saline (PBS) containing 2 mM ethylenediaminetetracetic acid (EDTA, pH 8.0) and was lysed by sonication (5 s on/off, 25% amplitude, 5 min). The insoluble fraction including the VFT was collected by centrifugation (12,000g, 30 min, 4 °C) and was solubilized in solubilization buffer [0.1 M Tris−HCl, 20 mM sodium dodecyl sulfate (SDS), 100 mM dithiothreitol, 1 mM EDTA, pH 8.0] at 30 °C overnight. The solubilized sample was centrifuged (12,000g, 30 min, 30 °C) and was collected. The sample was dialyzed in dialysis buffer [0.1 M sodium phosphate, 10 mM SDS, pH 8.0] using a MEMBRA-CEL dialysis membrane (Viskase) of 14 kDa molecular weight cut-off (MWCO). After filtering, the dialyzed sample with a 0.45 μm bottle top filter (Thermo Fisher Scientific), the sample was loaded to a 5 mL HisTrap affinity column (GE Healthcare) equilibrated with binding buffer [0.1 M sodium phosphate, 10 mM SDS, pH 8.0]. The column was then gradually washed with a washing buffer [0.1 M sodium phosphate, 10 mM SDS, pH 7.0]. Finally, the T1R2 VFT or T1R1 VFT was eluted with elution buffer [0.1 M sodium phosphate, 10 mM SDS, pH 6.0] and was stored at −80 °C for later use.

The SW or Rho were produced from *E. coli* similar to the previous

production process. The purified protein was stored at -80 °C for later use and thawed for an hour at 4 °C before use. The buffer of the purified SW and Rho was changed to HEPES buffer I [20 mM HEPES, 100 mM NaCl, 25 mM cholate, pH 8.0) using HiTrap™ Desalting column (GE Healthcare) for further assembly into NDs.

3.2.2 Expression and purification of membrane scaffold protein in *E. coli*

For membrane scaffold protein production, the Rosetta™ *E. coli* (DE3) strain was transformed with the pMSP1E3D1 bacterial expression vector by heat shock reaction and cultured under agitation in LB medium with kanamycin (50 μg/mL) at 37 °C until an OD600 value of 0.5 was reached. After induction with 0.5 mM IPTG and further culture for 4 h, the cells were harvested by centrifugation at 4 °C (7000×g, 20 min) and resuspended in buffer containing 20 mM Tris-HCl, 20 mM imidazole, and 0.5 M NaCl (pH 8.0). Then, they were lysed by sonication at 4 °C (30% amplitude, 5 s on/off, 5 min) and centrifuged at 4 °C (12000×g, 30 min). The supernatant containing soluble MSP1E3D1 was filtered through a 0.45 μm bottle top filter. The filtered sample was loaded onto a 5 ml HisTrap affinity column equilibrated with binding buffer [20 mM Tris-HCl, 0.5 M NaCl, 20 mM imidazole, pH 8.0]. After washing the column with wash buffer [20 mM Tris-HCl, 0.5 M NaCl, 50 mM imidazole, pH 8.0], His-tagged MSP1E3D1 was purified using elution buffer [20 mM Tris-HCl, 0.5 M NaCl, 350 mM imidazole, pH 8.0]. Buffer exchange with HEPES buffer I [20 mM HEPES, 100 mM NaCl, 1 mM EDTA, 20 mM cholate, pH 8.0] was performed using a HiTrap HP desalting column (GE Healthcare) for later use of ND assembly. The purified protein was stored

at -80 °C for later use and thawed at 4 °C for an hour before use. For additional process to remove the His tag from His-tagged MSP1E3D1, eluted MSP1E3D1 was mixed with TEV protease at a molar ratio of 1:100 at 4℃ for 16 h. MSP1E3D1without His tag was collected from the flow-through of a HisTrap™ HP column.

3.2.3 SDS-PAGE analysis

SDS-polyacrylamide gel electrophoresis (SDS-PAGE) and western blot analysis was performed. For SDS-PAGE, protein samples were incubated with a staining solution [Coomassie blue 0.5 g/L, acetic acid 7% (v/v), methanol 40% (v/v)] for 1 h at room temperature. The stained gel was incubated with a destaining solution I [acetic acid 7% (v/v), methanol 40% (v/v)] for 1 h at room temperature and then incubated with a destaining solution II [acetic acid 7% (v/v), methanol 5% (v/ v)] overnight at room temperature. For western blot, protein samples were mixed with a 2× Laemmli sample buffer added with 2-mercaptoethanol (Bio-Rad) and boiled for 5 min at 95 °C. After loading the samples and protein markers into the gel, SDS-PAGE was performed at 80 V. Protein bands were transferred to a nitrocellulose membrane, and the membrane was incubated with a blocking solution [5 wt% skim milk in PBS-T (1× PBS, 0.1 vol% Tween-20)] at room temperature for 1 h. An anti-His mouse antibody (Santa Cruz Biotechnology) was used as a primary antibody, and an HRP conjugated goat anti-mouse IgG antibody (Merck) was used as a secondary antibody. For analysis of SW-expressing mammalian cells, an anti-Rho rabbit antibody (Santa Cruz Biotechnology) was used as primary antibody, and an anti-rabbit IgG-HRP antibody was used as a secondary antibody. After washing the membrane several times with PBS-T, the protein band of the T1R2

VFT was analyzed using a TOPview ECL Pico Plus Western Substrate (Enzynomics).

3.3 Expression of photoreceptors in mammalian cells and construction of HEK-293 stable cell lines expressing photoreceptors

3.3.1 Expression of photoreceptors in HEK-293 and R28 cell

HEK-293 cells were maintained in Dulbecco's Modified Eagles Medium (DMEM) (HyClone, USA) supplemented with 1% penicillin, 1% streptomycin (Gibco, USA) and 10% Fetal Bovine Serum (FBS) (Gibco, USA) at 37°C under 5% CO_2 condition. The cells were transfected using Lipofectamine3000 (Invitrogen, USA) following the manufacturer's instruction. The cells were either used for fluorescence imaging or further used for SDS-PAGE analysis by sonication (2 s on/off, 2 min) (Sonics Vibracell, USA).

3.3.2 Lentiviral production and transduction of primary neuronal cells expressing photoreceptors

Approximately 2.2 × 10^6 HEK 293FT cells were cultured in 100 mm dishes of Dulbecco's modified Eagle medium (DMEM) (Biowest, France) supplemented with 10% fetal bovine serum (FBS), 1% penicillin, G418 (500 μg/ml) and GlutaMAX™ (Gibco, US) at 37°C under 5% CO_2. For production of virus stocks, 3 μg of lentiviral construct pCDH-CMV-Rho tag-SW-RFP-EF1-Puro or pCDH-CMV-Rho tag-Rho-RFP-EF1-Puro was transiently cotransfected with packaging plasmids 2.7 μg of pLP/VSVG, 4.5 μg of pLP1, and 1.8 μg of pLP2 into HEK 293FT cells using Lipofectamine 3000 reagent (Invitrogen, US). After 24-48 hours, the supernatant that contained the virus was harvested. Each vector was diluted in fully neurobasal medium and placed on SpheroFilm. After incubating for 24 hours, the medium with vector was

fully washed out with fresh medium.

3.3.3 Construction of HEK-293 stable cell lines expressing photoreceptors

HEK-293 cells were seeded to be 70% confluent the following day and cultured in complete medium at 37°C with 5% CO_2. The medium was replaced with fresh complete medium containing 5 μg/mL polybrene for increase in transduction efficiency. The produced lentivirus stock was added with an appropriate amount to obtain desired MOI and incubated at 37°C with 5% CO_2. The medium was replaced with fresh complete medium containing puromycin for antibiotic selection. After replacing fresh puromycin-containing medium every 3 days, the puromycin-resistant colonies were obtained. The cells expressing SW or Rho contain red fluorescence protein, RFP. Therefore, the cells expressing RFP were sorted using fluorescence-activated cell sorting (FACS).

3.3.4 Calcium imaging analysis

Photoreceptor gene-transfected cells were incubated with 5 μM fluo-4 AM (Molecular Probes, USA), 2.5 mM probenecid, and 10 μM 11-*cis*-retinal (Santa Cruz Biotechnology, USA) in Ringer's solution [140 mM NaCl, 1 mM $MgCl_2$, 1.8 mM $CaCl_2$, 5 mM KCl, 5 mM glucose, 10 mM HEPES (pH 7.4)] at 37°C for an hour. The cells were washed three times using Ringer's solution and further incubated in Ringer's solution for 30 min to completely de-esterify AM esters and remove nonspecific binding. The cells were imaged with a

fluorescence microscope and the intracellular Ca^{2+} intensity were measured at the emission wavelength of 525 nm, upon excitation wavelength of 480 nm. All experiments were performed in the dark.

3.4 Functional reconstitution

3.4.1 Refolding of T1R2 VFT and T1R1 VFT

The purified T1R2 VFT or T1R1 VFT was diluted to a concentration of 0.5 mg/mL and dialyzed in HEPES buffer I 20 mM HEPES, 10 mM SDS, 0.5 mM EDTA, pH 8.0] with a MEMBRA-CEL dialysis membrane (Viskase) of 14 kDa MWCO at room temperature. The dialysis buffer was then changed to HEPES buffer II [20 mM HEPES, 5 mM SDS, 0.5 mM EDTA, pH 7.5] at room temperature. Then, the buffer was replaced by HEPES buffer III [20 mM HEPES, 3 mM SDS, 0.5 mM EDTA, pH 7.5] at room temperature. 10 mM methyl-β-cyclodextrin was added to the dialyzed protein sample and stirred at 4°C overnight. The mixed sample was dialyzed in refolding buffer [20 mM HEPES, 1 mM EDTA, and 150 mM NaCl, pH 7.5] at 4°C.

3.4.2 Assembly of photoreceptor NDs

The lipid material was prepared by mixing 1-palmitoyl-2-oleoylphosphatidylcholine (POPC) and 1-palmitoyl-2-oleoylphosphatidylglycerol (POPG) (Avanti Polar Lipids) in a ratio of 3:2. The residual chloroform solvent in the lipid solution was removed by using nitrogen gas and then placing the sample in a vacuum desiccator overnight. The dried lipid film was then solubilized in cholate buffer (20 mM HEPES, 100 mM NaCl, 1 mM EDTA, 100 mM cholate, pH 8.0) under agitation. To reconstitute the SW- and Rho-NDs, respectively, the photoreceptor:MSP:lipid molar ratio was set at 0.1:1:75. The final concentrations of the mixture were 10 μM photoreceptor, 100 μM MSP1E3D1, 7.5 M lipids. The lipids, purified SW or Rho proteins and MSP were added in order, and the mixture was incubated for 2 h at 4°C. Bio-Beads (Bio-Rad), nonpolar polystyrene

adsorbents, were added to the mixture to absorb the detergent and incubated at 4°C overnight. After removing the Bio-Beads, the mixture was loaded onto an S200 size-exclusion column (Superdex 200 Increase 10/300 GL, GE Healthcare) equilibrated with HEPES II buffer (20 mM HEPES-NaOH, 100 mM NaCl, 1 mM EDTA, pH 8.0) to remove unbound proteins. Five hundred microliters of sample were injected at a flow rate of 0.5 mL/min. The ND fractions were collected and stored at 4°C.

3.4.3 Tryptophan fluorescence quenching assay

The ligand binding function of the functionally reconstituted protein was analyzed by a tryptophan fluorescence quenching assay using an LS 55 Luminescence spectrometer (PerkinElmer). The concentration of T1R1-VFT used for tryoptophan fluorescence quenching assay was 7.5 μM. The intrinsic tryptophan fluorescence of the protein was measured with excitation at 290 nm and emission at 350 nm. The relative fluorescence intensity was calculated with the formula $\Delta F/F_0$ (%) = $[(F_0 - F)/F_0] \times 100$. F_0 and F refer to the fluorescence intensity of the receptor before and after the treatment of ligand molecules, respectively.

3.4.4 Dynamic light scattering and scan electron microscopy imaging

The size of the photoreceptor NDs was analyzed by a DLS spectrophotometer (DLS-7000). Field-emission scanning electronic microscopy (AURIGA, Carl Zeiss) was used to analyze the size and morphology of photoreceptor NDs.

3.5 Fabrication of ligand binding domain of human taste receptors immobilized on CNT-FET sensors

3.5.1 T1R2 VFT immobilization on CNT-FET

A CNT-FET device was incubated in an N-acetyl-L-cysteine solution (0.5 M in distilled water) for 12 h at room temperature. The chip was gently rinsed with distilled water. The device was incubated with a mixture of EDC (20 mM in MES buffer) and NHS (40 mM in MES buffer) for 30 min. The chip was gently rinsed with HEPES buffer. Then, 1 μL of T1R2 VFT in a HEPES solution was dropped on the channel region of the sensor. The sensor was incubated for 2 h at room temperature. The prepared chip was stored at 4°C. The chip was washed to remove unbound protein before each measurement.

3.5.2 T1R1 VFT immobilization on CNT-FET and formation of hydrogel layers on T1R1 VFT-based sensors

A CNT-FET device was incubated in an N-acetyl-l-cysteine solution (0.5 M in distilled water) for 12 h at a room temperature, and the chip was gently rinsed with distilled water. Then, the chip was incubated with a mixture of EDC (20 mM in MES buffer) and NHS (40 mM in MES buffer) for 30 min and gently rinsed with a HEPES buffer. Afterward, it was incubated with 1 μL of T1R1-VFT in a HEPES solution for 2 h at a room temperature and gently rinsed with HEPES buffer to remove unbound protein. The concentration of T1R1-VFT used for immobilization on CNT-FET device was 60.4 μM.

The PAAm hydrogel was prepared according to a previously-reported method. Briefly, AAm monomer powder (2.17 M) and 0.06 wt% N, N-

methylenebisacrylamide (MBAA) (with respect to the AAm) as a cross-linker were dissolved in deionized water to obtain an aqueous solution. Then, LiCl (4 M) and 0.16 wt% ammonium persulfate (APS) as an initiator were added into the aqueous solution. After sonicating and degassing the mixture in a vacuum chamber, 0.25 wt% N, N, N′, N′-tetramethylethy-lenediamine (TEMED) with respect to the AAm was further added as an accelerator. Finally, 0.2 uL of hydrogel solution was dropped on the channel region, and the chip was placed at a room temperature for 30 min so that a hydrogel layer was formed on the chip surface. The prepared chip was stored at 4°C for a future usage.

3.6 Fabrication of PDMS and photoreceptor ND-filled waveguides

3.6.1 Refractive index measurement of photoreceptor NDs

The refractive index of the photoreceptor NDs was determined using a liquid refractometer. Seven wavelengths in the visible light region from 500 to 800 nm separated by intervals of 50 nm were utilized for effective experiments; this range spans from blue to near infrared emissions for matching with photoreceptor's spectral sensitivity according to human vision and avoiding overlap among spectra. These beams were filtered from the white light of a supercontinuum source (SuperK Compact, NKT Photoniks) using monochromatic filters (FMiSM, IISM) with an average FWHM of approximately 3 nm and a relative standard deviation of approximately 4%.

Using the displacement δ of the beam and the incident angle θ to the cuvette surface, we can calculate the refractive index of the liquid in the cuvette with equation (2).

$$n = n_o \sin\theta \sqrt{1 + \left[\frac{\cos\theta}{\sin\theta - \Delta / d} \right]^2} \tag{2}$$

where n_o is the air refractive index, d is the path length of the cuvette, and $\Delta = \delta - \delta_o$ is the displacement of the Gaussian peaks between the liquid-filled cuvette and the empty cuvette. The peak locations were obtained by Gaussian fitting of the measured data using 'OriginPro 9.0' program, which were detected from the knife edge system as usual beam shape measuring method. With different incident angles (θ) from 10 to 40°, we measured the displacements and determined the refractive index by averaging all the results.

3.6.2 Fabrication of photoreceptor ND-filled PDMS-based waveguides and analysis of beam profile intensity

A waveguide was fabricated using polydimethylsiloxane (PDMS) (silicone elastomer kit, Sylgard 184 A/B, Dow Corning) based mold structured constructed by 3D printer (Creality 3D CR-10S Pro, Creality). The PDMS solution was cured in the mold overnight after reducing bubbles in a vacuum desiccator. The most favorable structure with a width:gap ratio of 1:2 in the PDMS grooves was chosen. The surface for the focusing beam was constructed to be flat and perpendicular to the beam-propagation axis, and the opposite surface for the emitting beam had a round shape, which reduced the bias refraction. After filling the empty space of "width" in the PDMS grooves with 200 μl of the liquid dispersion of NDs, we observed the refracted beam on the screen located 10 cm from the output surface. Images were captured by a digital camera (V40 ThinQ, LG) to investigate the beam profile spreads on the screen. The images were analyzed by using MATLAB and color-coded based on #ff0000 for red. With the screen in the same position, we also measured the beam intensity by utilizing a power meter (PM100D, Thorlabs) as a photodetector to observe the intensity variation over time.

Chapter 4

Production of ligand binding domain of human sweet and umami taste receptors

4.1 Introduction

Animals, including human, can discern nutrition through sensation of sweet and umami tastes. Sweet and umami tastes are perceived as 'palatable' taste by human through the taste receptor type 1 (T1R) family. Sweet and umami taste receptors are heterodimeric class C GPCRs in the T1R family; T1R2/T1R3 is sweet taste receptor and T1R1/T1R3 is umami taste receptor. Class C GPCRs are composed of three subunits: extracellular ligand-binding domain (Venus flytrap (VFT)), cysteine rich domain (CRD), and transmembrane domain (TMD). T1R2 VFT and T1R1 VFT are known to play a significant role in ligand binding. The primary step in taste recognition is the binding of taste molecules to a taste receptor, which then activates the receptors for subsequent reactions. Therefore, researcher have taken a keen interest in taste receptors, not only in understanding the structure-function relationship, but also utilizing taste receptors to detect taste compounds for food, beverage and pharmaceutical applications.

GPCRs have been reported to be difficult to overexpress, solubilize and purify due to their complex structures and strong hydrophobicity, and it is difficult to obtain sufficient amount of purified GPCRs for ligand binding studies. Although the bacterial expression system is known to be more efficient than the mammalian expression system in terms of high-level protein production, the sweet taste receptor, which has a heterodimeric, large and complex structure, is difficult to be expressed.[1,2]

In this chapter, the T1R2 VFT and T1R1 VFT, a primary ligand-binding domain of a human sweet and umami taste receptor, were produced from *E. coli* as an alternative strategy to using a whole receptor. The VFT and T1R1 VFT, which have been purified and functionally refolded, can be used to detect

tastants in a relatively simple way using tryptophan fluorescence assay, and furthermore, and they can also be combined with nanomaterials to develop bioelectronics tongues.

4.2 Expression and purification of ligand binding domain of human sweet and umami taste receptors in *E. coli* system

The ligand binding domain of human sweet and umami taste receptors, T1R2 VFT and T1R1 VFT, were expressed and purified from *E. coli.* **Figure 4.1** shows the SDS-PAGE gel staining and western blot analysis of the purified T1R2 VFT and T1R1 VFT. The elution peak of FPLC elution profile and SDS-PAGE gel staining and western blot analysis in the steps of after cell lysis, solubilization, and purification are shown in **Figure 4.2**. The gel staining and western blot analysis showed bands at 54 kDa for T1R2 VFT and 53 kDa for T1R1 VFT, which corresponds to the molecular weight calculated by the online ExPASy bioinformatics tool. These results indicate that both T1R2 VFT and T1R1 VFT were successfully overexpressed and purified. It is well known that expressing a full class C GPCRs, such as a human sweet taste receptor, is difficult, and that even expressed GPCR frequently demonstrate poor functionality due to their large size and complex heterodimeric structure. VFTs of human sweet and umami taste receptors, have been identified to have the desired functionality for primary ligand binding and initiating receptor responses.[2,47]

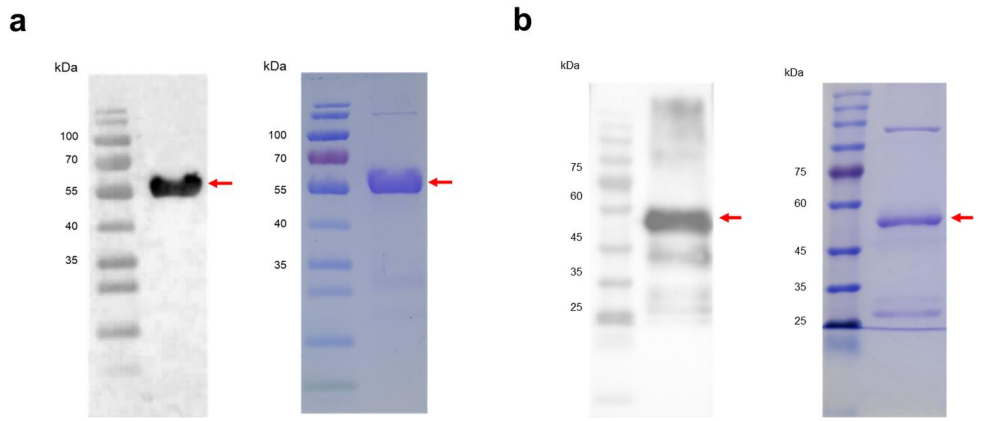

Figure 4.1 SDS-PAGE analysis of purified (a) T1R2 VFT and (b) T1R1 VFT from *E. coli*

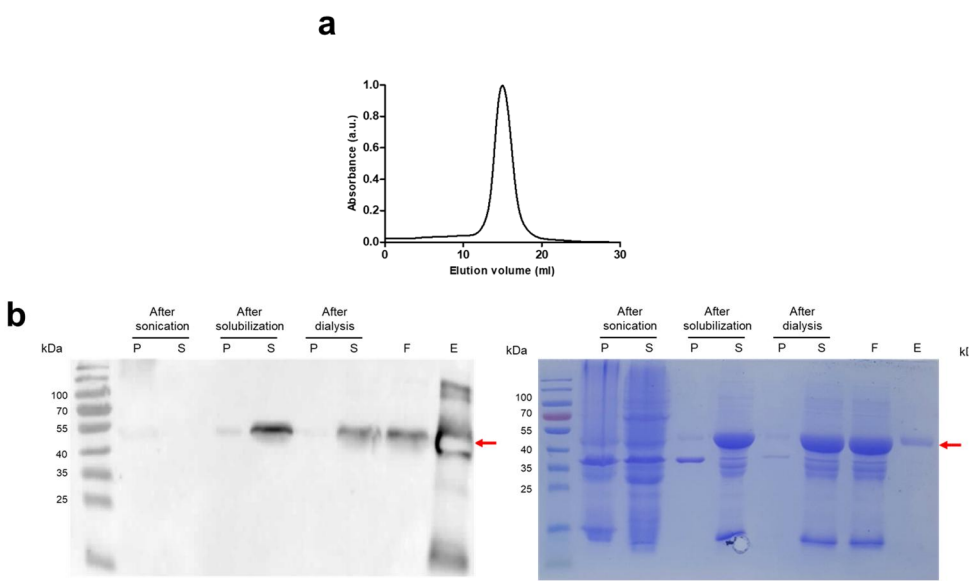

Figure 4.2 Purification of T1R2 VFT expressed in *E. coli*

(a) Fast protein liquid chromatography (FPLC) elution profile of T1R2 VFT. (b) SDS-PAGE analysis of T1R2 VFT after cell lysis, solubilization, and purification. P: pellet after centrifugation; S: supernatant after centrifugation; F: filtrate; E: eluent.

4.3 Functional characterization of ligand binding domain of human sweet and umami taste receptors

The ligand binding functionality of the refolded T1R2 VFT and T1R1 VFT were examined using a tryptophan fluorescence quenching assay. Tryptophan residues in proteins exhibit intrinsic fluorescence at emission wavelengths around 350 nm. As ligands bind to the receptor protein, conformational changes occur and can reduce the fluorescence intensity.[48,49] The sweet substances bind to T1R2 VFT, while the umami compounds bind to T1R1 VFT, causing conformational changes in the receptor and fluorescence quenching of tryptophan residues. As shown in **Figure 4.3**, sucrose was used as the representative sweet tastant to evaluate the ligand-receptor binding functionality. The change in relative fluorescence intensity increased with increasing sucrose concentration. As sucrose concentration increased, the change of relative fluorescence intensity also increased. This result shows the T1R2 VFT responds to sucrose in a dose-dependent manner, implying that the receptor was functionally refolded.

For functionality test of T1R1 VFT, MSG was used as the representative umami taste compound(**Figure 4.4**). The relative fluorescence intensity increased as MSG concentrations increased. The results showed that the T1R1-VFT responds to umami substances, therefore it was properly refolded and retained its original functionality.

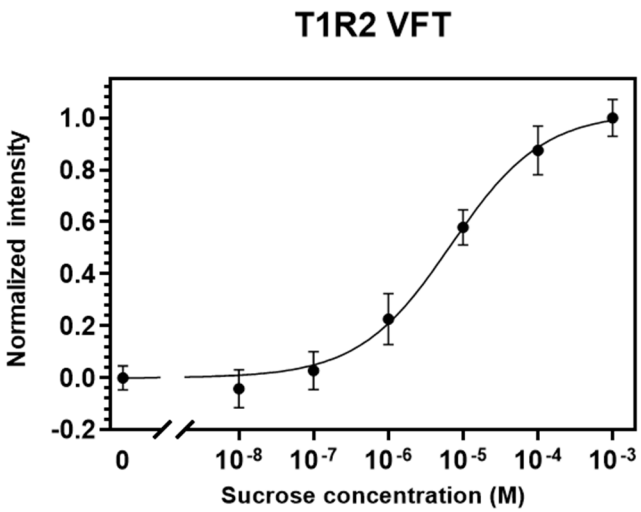

Figure 4.3 Functionality test of T1R2 VFT to sucrose using tryptophan fluorescence quenching assay

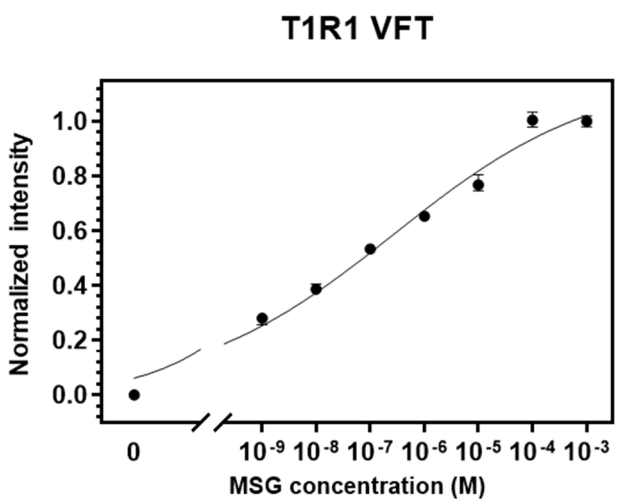

Figure 4.4 Functional assay of T1R1 VFT to MSG using tryptophan fluorescence quenching assay

4.4 Conclusions

In this study, the T1R2 VFT and T1R1 VFT, a primary ligand-binding domain of a human sweet and umami taste receptor, were successfully produced from *E. coli* as an alternative strategy to using a whole receptor. T1R2 VFT and T1R1 VFT, purified from *E. coli*, was evaluated with western blot analysis and SDS-PAGE gel staining, indicating a high yield and high purity. T1R2 VFT and T1R1 VFT purified samples were refolded to regain their original function. The functions were assessed using a tryptophan fluorescence assay, and both T1R2 VFT and T1R1 VFT responded to their representative tastants, sucrose and MSG. Both demonstrated a dose-dependent response, implying that the receptor has been functionally refolded and is ready to be used as biomaterials for detecting sweet and umami substances.

Chapter 5

Ligand binding domain of human sweet taste receptor: Analyses and applications to measure sweet taste

5.1 Introduction

Recognizing sweet substances is critical for the human and animal survival in terms of managing caloric intake and contributing to dietary choices.[50,51] The sweetness sensation is derived from carbohydrates, which is the primary energy source in the human diet. However, an excessive carbohydrate intake is considered a serious issue in modern society, which can lead to chronic diseases such as obesity, diabetes, hypertension, and metabolic syndrome.[52-54] As a result of the rising demand for calorie-free sweeteners, research and development of calorie-free sweeteners and sweetness modulators is gaining prominence. As a result, it is important to evaluate the sweet substances in food for various fields such as healthcare, food, and pharmaceutical industries.

Various methods for detecting and evaluating sweet substances have been developed. Human sensory evaluation is the most commonly used method, however, there are several limitations, such as a slow test speed and individual variation in taste sensitivity.[55] Accordingly, there is a growing interest in taste, and various methods for objectively evaluating sweet substances have been developed over time. High-performance liquid chromatography,[56,57] sensors using lipid polymer membrane,[58] electrochemical methods,[59] and surface plasmon resonance spectroscopy are examples of such methods.[60] Although these techniques were successful in detecting sweet substances analytically, they featured low selectivity and could not reproduce versatile natural aspects of the human taste system, such as the synergistic effect between sweeteners.[61]

In recent years, bioelectronic tongues have been developed to combine the benefits and overcome the limitations of human sensory evaluation and conventional measurement methods. Nanovesicle-based[45,46] and receptor

protein-based[62-64] artificial taste sensors are the examples. Nanovesicle-based bioelectronic tongues, in particular, could mimic the natural environment in cells and allowed to use a full functional membrane receptor. However, it remains difficult due to the complicated production and low protein expression yield using mammalian cells. On the other hand, receptor protein-based bioelectronic tongues can facilitate high-level production of proteins using bacterial expression and hold superior advantages in stability and reusability.[44] Furthermore, the detection limit of receptor-based devices was lower detection limit than that of nanovesicle-based devices, which had a detection limit of a micromolar level.[45,46] Bioelectronic tongues are constantly developing, and further advancements should focus on the practical application and development of commercial devices. Therefore, receptor protein as biorecognition elements for bioelectronics tongue can be more practical choices than other biomaterials, such as nanovesicles, tissues, cells, and enzymes.

Sweet taste can be objectively evaluated and standardized by mimicking biological taste sensation.[65] The primary step in taste recognition is the binding of taste molecules to a taste receptor, which then activates the receptors for subsequent reaction. In particular, T1R2 VFT of human sweet taste receptor are known to play a significant role in ligand binding. Different strategies of overexpress and produce subunits of taste receptors have been focused on investigating the structure-function relationship of taste receptors. Due to the large and complex structure, a sweet taste receptor, which is a class C GPCR, is difficult to express in bacterial systems. Therefore, utilizing T1R2 VFT as a biomaterial for detecting sweet substances can benefit the evaluation and standardization of sweet taste. T1R2 VFT can be used to detect sweet taste in

a relatively simple way using tryptophan fluorescence assay, and furthermore, they can also be combined with nanomaterials to develop bioelectronics tongues .

In this chapter, the T1R2 VFT produced from *E. coli* was used for analysis and practical application to evaluate sweet taste. The taste ligand efficacy of T1R2 VFT to various sweet taste ligands was measured using tryptophan fluorescence quenching assay. Moreover, T1R2 VFT was immobilized on the floating electrodes of a carbon nanotube field-effect transistor (CNT-FET). Sweet substances and real beverage samples were tested using the T1R2 VFT-functionalized bioelectronic tongue.

5.2 Taste ligand efficacy analysis in ligand binding domain of human sweet taste receptor using a tryptophan fluorescence assay

The dose-dependent response of T1R2 VFT to various sweet tastants were examined using a tryptophan fluorescence quenching assay. The sweet substances bind to T1R2 VFT, causing conformational changes in the receptor and fluorescence quenching of tryptophan residues. As shown in **Figure 5.1**, the change of relative fluorescence intensity increased along with the sweetener concentration. Dose-reponse curves were fitted using the Hill equation for sigmoidal curves to allow for a more accurate comparison of ligand efficacy among different sweeteners. Relative sweetness, also known as sweet potency, is a term used to describe the sweetness of different sweeteners in sensory evaluation. It also serves as a quick indicator of the sweetener concentration needed to achieve an equivalent sweetness intensity to the standard sucrose concentrations. A sweetener could be regarded as "more potent" than sucrose if its sweetness potency is greater than 1, which means that a lower

concentration of the sweetener is needed to produce the equivalent sweetness intensity at a certain sucrose concentration.[66,67] Given that relative sweetness can be defined as a ratio of sucrose concentration to that of a sweetener at equivalent sweetness intensities, the relative sweetness from tryptophan assay was calculated using the formula equation (1):

$$\text{Measured relative sweetness} = \frac{\text{Concentration of sucrose}}{\text{Concentration of sweetener at equivalent relative fluorescence intensity to sucrose}} \quad (1)$$

where measured relative sweetness is calculated using the sucrose and sweetener concentrations converted and expressed in % w/v as used in sensory evaluation. As shown in **Figure 5.1**, the horizontal dashed line was plotted to indicate the equivalent relative fluorescence intensities of sweeteners to 10^{-3} M sucrose. The sucrose concentration was set to 10-3 M because the difference in concentration of sweeteners at equivalent relative fluorescence intensity to sucrose was greatest at this concentration. Since the relative fluorescence intensity at 10^{-3} M was not obtained, glucose was not included in the comparison to sucrose. **Table 5.1** shows the concentration of sweetener at equivalent relative fluorescence intensities to sucrose in molar concentration (M) and weight per volume percent (% w/v). 3.42E-02% w/v sucrose and each sweetener concentration at equi (% w/v) were inserted into the equation (1), and the relative sweetness of each sweetener was calculated. The relative sweetness as measured by the tryptophan fluorescence assay could provide a quick and simple way to interpret ligand binding at the receptor level. Moreover, the measured relative sweetness showed a similar result to a human perception, where other sweeteners are perceived as 'more potent' than sucrose.

Figure 5.2 shows the tryptophan fluorescence quenching assay results using

various taste molecules. The 1 μM addition of sucrose, fructose, glucose, aspartame, and saccharin changed fluorescence intensities by 12−15%. On the other hand, relative fluorescence intensity changes were less than 3% when sodium cyclamate (cyclamate, artificial sweetener), cellobiose (tasteless disaccharide), monosodium glutamate (MSG, umami tastant), and denatonium benzoate (denatonium, bitter tastant) were introduced. No significant fluorescence change was detected by using cyclamate which is an artificial sweetener known to interact with the TMD of T1R3.[17] The results indicate that the produced T1R2 VFT can selectively recognize sweet substances among various taste molecules.[17,18]

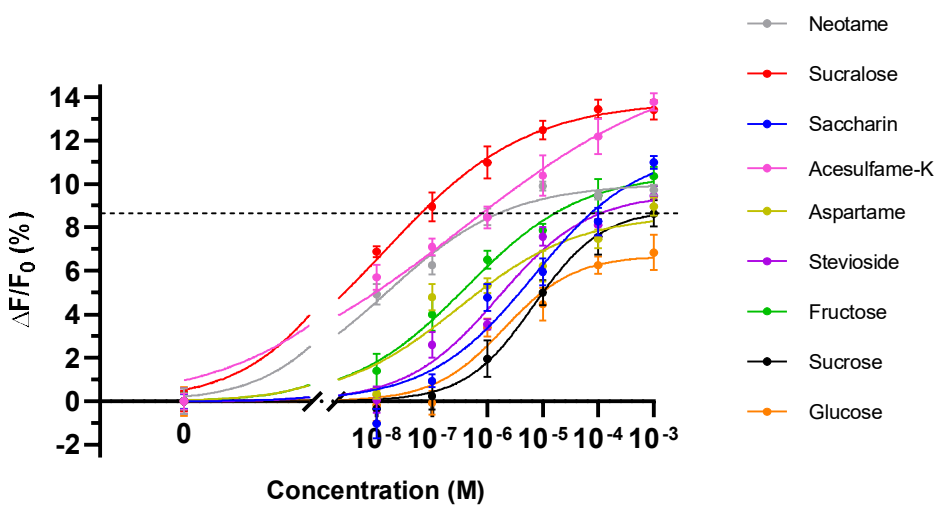

Figure 5.1 Dose-dependent responses of T1R2 VFT to various sweet taste molecules using tryptophan fluorescence quenching assay

The horizontal dashed line indicates the equivalent relative fluorescence intensities of sweeteners to 10^{-3} M sucrose.

Sweetener	Concentration of sweetener at equi (M)	Concentration of sweetener at equi (%wv)	Measured relative sweetness
Sucralose	6.27E-08	2.49E-06	1.37E+04
Acesulfame-K	7.93E-07	1.60E-05	2.14E+03
Neotame	1.58E-06	6.00E-05	5.71E+02
Fructose	1.62E-05	2.91E-04	1.18E+02
Saccharin	7.31E-05	1.34E-03	2.56E+01
Stevioside	1.09E-04	8.81E-03	3.89E+00
Aspartame	1.00E-03	2.94E-02	1.16E+00
Sucrose	**1.00E-03**	3.42E-02	**1.00E+00**

Table 5.1 Comparison of sweetener concentrations at equivalent fluorescence intensities to sucrose and their measured relative sweetness using tryptophan fluorescence assay

Concentration of sweetener at equi: concentration of sweetener at equivalent fluorescence intensity to 10^{-3} M sucrose using tryptophan fluorescence assay

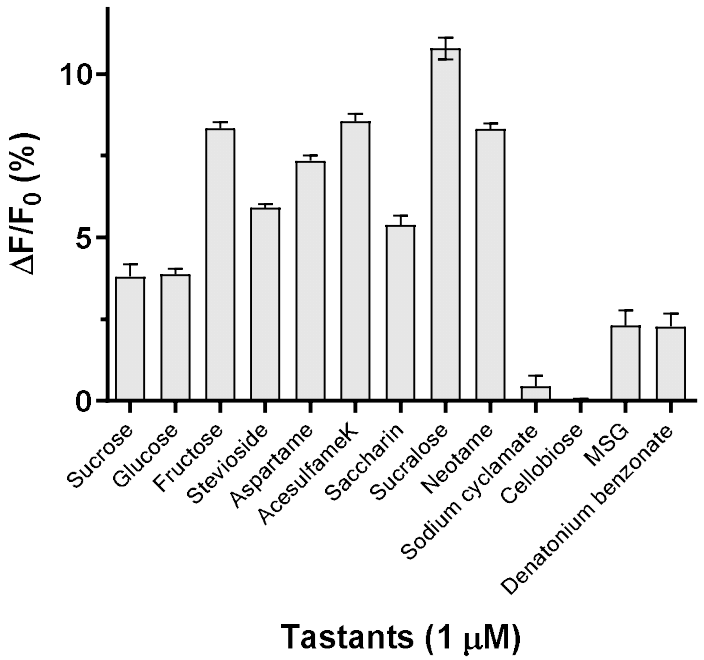

Figure 5.2 Selective responses of T1R2 VFT to sweet taste molecule using tryptophan fluorescence quenching assay

Data are expressed as means ± standard deviation (n = 5).

5.3 Fabrication and characterization of T1R2 VFT-based CNT-FET

The schematic diagram of a floating electrode-based bioelectronic tongue using the T1R2 VFT is shown in **Figure 5.3**. In this study, T1R2 VFT was used as a recognition bioelement to develop a practical biosensor for detecting sweet taste. T1R2 VFT was selectively immobilized on floating electrodes of the CNT-FET via an amide bond using cysteine linker.

Figure 5.4a depicts a scanning electron microscopy (FE-SEM) image of the T1R2 VFT-immobilized CNT-FET. Between the source and drain electrodes, floating electrodes and a CNT channel were constructed. In the enlarged image of **Figure 5.4a**, the bright region is the T1R2 VFT-immobilized gold floating electrodes, and the dark region is the CNT channel.

AFM topography images of floating electrodes before and after functionalization of the T1R2 VFT are shown in **Figure 5.4b**. The T1R2 VFT-immobilized gold electrode had several spots, while the bare electrode had a pristine surface. The spots are estimated to be 12.6± 8.1 nm in size, which corresponds to the size of the T1R2 VFT in previous literature.[68] The results show that the T1R2 VFT was successfully immobilized on the surface of the device. “Such a high sensitivity can be attributed to the small size of T1R2 VFT receptor parts used in our device. Presumably, as small VFT domains can exist within the Debye length from the sensor surface, any electrical changes induced by the binding of sweet substances to the T1R2 VFT can more easily affect the conductance of the underlying CNT channels.”

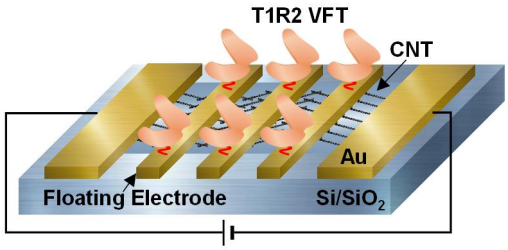

Figure 5.3 Schematic illustrations of a bioelectronic tongue based on T1R2 VFT for sweet taste detection

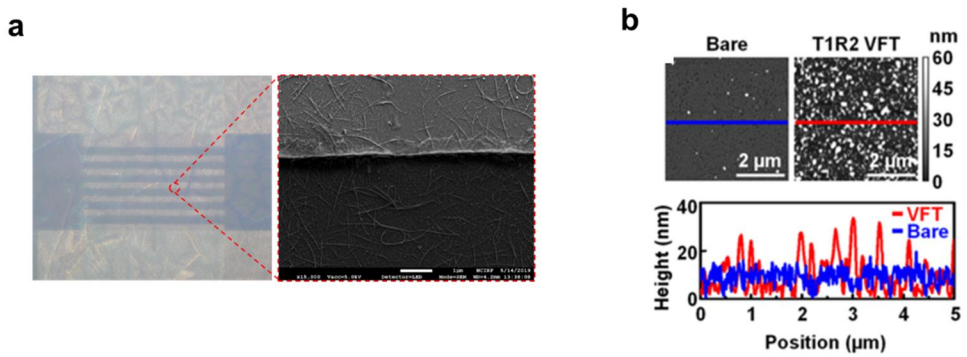

Figure 5.4 FE-SEM and AFM images with height profiles of T1R2 VFT immobilized on floating electrode of a CNT-FET

5.4 Detection of sweet tastants using T1R2 VFT-based CNT-FET

The conductance of the underlying CNT channel changes when sweet compounds bind to the T1R2 VFT on the floating electrode, enabling for real-time detection of sweet substances. As shown in **Figure 5.5a**, the real-time response of T1R2 VFT-immobilized device to various sucrose concentrations was examined. The source-drain current of a sensor was monitored in real time while target sucrose solutions were added. Throughout the experiments, a constant bias voltage of 0.1 V was maintained. When sucrose solutions were introduced into our sensor, the current decreased immediately. After some time, the current level was stabilized at a constant value. Notably, the sensor began to respond to the addition of 0.1 fM sucrose concentration. This detection limit implies the present device shows ~10^7 times higher sensitivity compared to previously reported sensors, including bioelectronic nose based on a whole receptor. [45,46,69] Since the small size of T1R2 VFT can exist within the Debye length from the electrode surface, any electrical changes caused by the binding of sweet substances to the T1R2 VFT can more easily affect the conductance of the underlying CNT channels. Therefore, the small size of T1R2 VFT is most likely to explain the sensor's high sensitivity.

Sweet substance binding can trigger conformational changes in the T1R2 VFT on the sensor's floating electrode and enable charge redistribution in the protein. Such charge redistribution in the T1R2 VFT modifies the work function (ϕM) of floating electrodes, which alters the Schottky barrier height (ϕSB) between the CNT channel and the floating electrode.[70,71] The increased Schottky barrier acts as an enhanced potential barrier to hole carriers, causing the CNT channel current to

decrease. As a result, sweet substance binding to the T1R2 VFT induces a current change in the device, enabling real-time detection of sweet compounds.

Normalized signals of the devices to various concentration of sucrose and saccharin solutions are shown in **Figure 5.5b**. The sensing measurements for three devices were carried out to obtain mean values and error bars. The normalized signals were generated by normalizing the current changes in relation to their maximum values. The response curves were further analyzed by using the Hill equation.[40,41] The normalized signal N of a device can be written by the Hill equation like

$$N = \frac{C^n}{K_d^n + C^n} \quad (2)$$

where C, n, and Kd are the concentration of sweet tastants, a Hill's coefficient, and a dissociation constant for tastants binding to T1R2 VFT, respectively. As a result, the dissociation constants of sucrose and saccharin to the T1R2 VFT were calculated to be 2.05×10^{-11} M (7.02×10^{-9} g/L) and 6.88×10^{-12} M (1.26×10^{-9} g/L), respectively. The dissociation constant of saccharin was three times lower than that of sucrose. Although in cell-based measurements, the efficacy of saccharin was substantially higher than that of sucrose.[72] Herein, the direct binding of sweet taste molecules and receptors was measured without the need of cellular signaling pathway. As a result, may differ from that measured by cellular tests. Although T1R2/T1R3 receptor exclusively transduces sweet taste, specific amino acid residues in the T1R2 VFT cleft areas that bind to different sweet substances may vary.[73,74] Furthermore, caloric and noncaloric sweeteners are observed to have distinct signaling pathways in taste bud cells.[75,76] In this study, the T1R2 VFT-based device could directly measure the conformational change of the T1R2 VFT, whereas

previous cell-based assays required complex signaling processes in the cells to obtain the signals.

Figure 5.6 shows the real-time response of the device to various taste molecules. A constant bias voltage of 0.1 V was maintained throughout the measurements. 1 μM solutions of cellobiose and MSG and 1 nM solution of sucrose were introduced to the sensor. Cellobiose is known as a tasteless sugar, whereas MSG is a representative umami taste substance. The addition of cellobiose and MSG solutions at relatively high concentration resulted in negligible conductance changes, whereas 1 nM sucrose solution resulted in a significant decrease in the conductance of the device. The highly selective response of the sensor can be explained by the highly selective binding of T1R2 VFT to sweet ligands.[17,77,78] The results show that the T1R2 VFT-based bioelectronics tongue could distinguish sweet substances from other non-sweet tastants with high selectivity similar to human tongue.

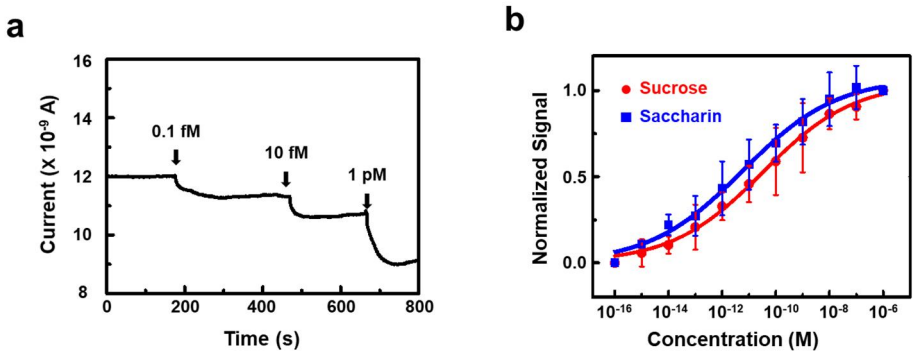

Figure 5.5 Responses of T1R2 VFT-based bioelectronics tongue to sucrose

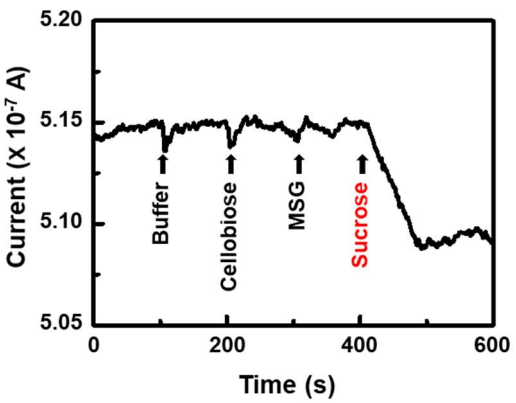

Figure 5.6 Selective responses of T1R2 VFT-based bioelectronics tongue to sucrose

5.5 Measurements of real beverage samples using T1R2 VFT-based CNT-FET

The T1R2 VFT-based bioelectronic tongue was tested with commercial beverage samples to prove its value in real sample analysis. Commercial juice and tea were tested using the device. In **Figure 5.7a**, the device showed

dose-dependent response to diluted apple juice. Commercial apple juice was serially diluted in a HEPES buffer solution, which contains various natural sweet compounds such as sucrose, glucose, and fructose at a total concentration of ~100 mg/mL. To obtain the normalized signals, the measured sensor signals were normalized with regard to their maximum values. The device began to respond at a diluted concentration of 10^{-16} (v/v), and the responses were saturated at around 10^{-4} (v/v). The EC_{50} value the device to apple juice was calculated by fitting the data using the Hill equation. The EC_{50} value was estimated to be 1.00×10^{-10} (v/v). Using the known saccharide concentrations in apple juice, the measured EC50 value by volume ratio may be converted to a mass concentration of 1.00 × 10−8 g/L, which is comparable to the responses of the device to sucrose in **Figure 5.5**. These results demonstrate the device can detect a trace amount of sweet substances in apple juice and can be used to evaluate commercial beverages for practical application.

Figure 5.7b shows the normalized responses of our device to chamomile tea with varying sugar concentrations. Herein, 100 mg/mL of sucrose was mixed with chamomile tea. The sucrose-added chamomile tea was serially diluted to generate solutions of varying concentrations and then added to the device. The sensing signals increased as the concentration of chamomile tea increased. The T1R2 VFT-based sensor could detect sucrose in chamomile tea, according to the results. The EC_{50} value for sucrose in chamomile tea, 1.89×10^{-8} g/L, was obtained using Hill equation and is comparable to the values in a buffer solution and apple juice.

Furthermore, the enhancing effect of chamomile tea on the T1R2 VFT activity was observed by comparing the responses to chamomile tea, sucrose solution, and sucrose-added chamomile tea (**Figure 5.8**). Chamomile tea was diluted in a HEPES buffer solution at a ratio of 1:1000. Sucrose solution was prepared in a HEPES buffer solution at a concentration of 0.3 mM. Sucrose-added chamomile tea was made by concentrating sucrose in diluted chamomile tea to 0.3 mM. In **Figure 5.8a**, $|\Delta G/G_0|$ represent absolute values of the relative conductance change, whereas G_0 and ΔG represent the device conductance before the addition of target solutions and the conductance change after the addition of target solutions, respectively. Chamomile tea had negligible effect on relative conductance, while a sucrose solution caused a 5.9% change. Sucrose-added chamomile tea, on the other hand, caused a much larger change of 21% in the device than a sucrose solution. These results suggest that chamomile tea greatly enhanced the sensor responses to sucrose. Similar results were obtained by tryptophan fluorescence assays shown in **Figure 5.8b**. Sucrose-added chamomile tea resulted in a much larger change in relative fluorescence intensity than chamomile tea or sucrose solution alone. Further identification of specific compounds in chamomile that enhance sweet sensation is required and is being investigated. Chamomile tea, on the other hand, is known to contain a variety of components such as amino acids, minerals, and polyphenols, which may influence the perception of sweetness.[79] For example, previous reports have shown that some amino acids in tea can enhance the sweet taste.[80] The real beverage sample test results indicates the T1R2 VFT-based sensor can be utilized to evaluate the sweet substances in various environments.

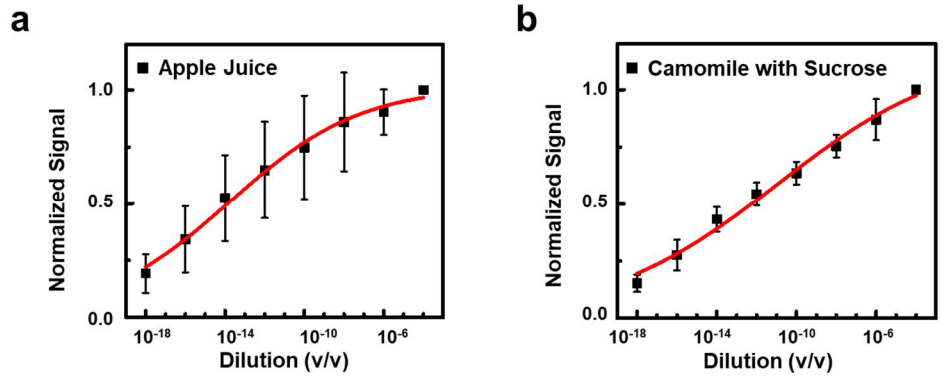

Figure 5.7 Dose-dependent responses of T1R2 VFT-based bioelectronic tongues to various beverage samples

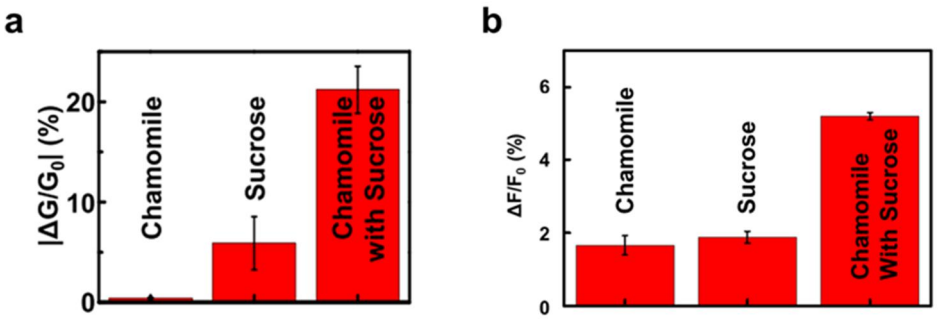

Figure 5.8 Relative conductance change of the device and tryptophan fluorescence of T1R2 VFT by the addition of sucrose with or without chamomile tea.

(a) Relative conductance change of the device (b) Relative tryptophan fluorescence intensity of T1R2 VFT by the addition of sucrose with or without chamomile tea. This result demonstrates the enhancement of sweet taste by chamomile tea.

5.6 Conclusions

The ligand-binding domain of the human sweet taste receptor was produced from *E. coli*, and various analyses and applications involving it were investigated. The efficacy of sweet taste substances was practically evaluated using tryptophan fluorescence analysis, which is a relatively simple method for evaluating sweet taste using ligand-binding domains of human sweet receptors. The sweet taste ligand efficacy analysis using a tryptophan assay could demonstrate the human-like selective responses of T1R2 VFT to sweet tastants. In particular, the relative sweetness as measured by the tryptophan fluorescence assay could provide a quick and simple way to interpret ligand binding at the receptor level. Although the tested sweetener concentration was below the human threshold, the measured relative sweetness showed a result similar to a human perception, where other sweeteners are perceived as 'more potent' than sucrose.

A T1R2 VFT was immobilized on the floating-electrode of a CNT-FET to develop an ultrasensitive bioelectronic tongue device for detecting sweet compounds. The device could detect sweet tastants down to 0.1 fM with high sensitivity and selectivity. The sensor could detect sweet compounds in commercial beverages such as apple juice and chamomile tea. The T1R2 VFT-based CNT-FET has the potential to be a powerful tool for the detection of sweet substances, as well as having a substantial application in the food sector and fundamental investigation.

Chapter 6

Ligand binding domain of human umami taste receptor: Analyses and applications to measure umami taste

6.1 Introduction

Umami taste, commonly known as a pleasant savory flavor, influences food preference and acceptance in human. It also exhibits a taste-enhancing synergism between two umami tasting chemicals, L-glutamate and 5'-ribonucleotides.[81] Umami taste satisfies the human's desire in foods, however excessive consumption of umami substances can lead to health concerns such as metabolic syndrome, obesity, and numbness.[82] Therefore, the demand for investigation of healthy umami taste seasoning has prompted the research in development of rapid and sensitive tools for the detection of umami tastants. Sensory evaluation methods, mass spectrometry, and electronic tongues are commonly utilized methods for detecting umami compounds.[83] Although sensory evaluation involves human perception, the procedure takes time and the outcomes can be subjective for each individual. Mass spectrometry and electronic tongues, are precise in quantifying umami components however, they have drawbacks such as complicated procedures and limited selectivity.[61,84]

The binding of taste molecules to a taste receptor, which activates the receptors for further reaction, is the first step in taste perception. T1R1 VFT of human umami taste receptor are known to play a significant role in ligand binding. Since the whole heterodimeric umami receptors with their large and complex structures are difficult to produce in bacterial systems, producing and using T1R1 VFT is an alternative. The use of T1R1 VFT as a biomaterial for detecting umami substances can contribute to the objectively evaluate and standardize umami taste. T1R1 VFT can be relatively simple and practical approach to detect umami taste with tryptophan fluorescence assay, or further combination with nanomaterials to produce bioelectronics tongues.

Several previous studies have used T1R1 VFT for biosensor applications T1R1

VFT-based FET was first developed for the detection of umami substances in real-time.[62] T1R1 VFT-hybridized devices were developed to improve device performance and stability utilizing the small size of the VFT.[85] Umami electrochemical biosensor of T1R1 VFT-immobilized AuNPs@ZIF-8/Ti3C2 MXene was developed for highly sensitive detection of umami compounds.[83] However, most sensors simply immobilize receptors on the surface of an electrode without any protective membrane, which can easily result in non-specific adsorption of macromolecules and misleading signals in practical sample detection. Furthermore, keeping such receptors stable on the surface of a nanostructure is difficult in vitro environment. After integration with sensors, receptors may lose their reactivity, resulting in a short sensor lifetime.

A polyacrylamide (PAAm) conducting hydrogel has been widely applied in sensors, electronic skins, and wearable devices for its good biocompatibility and fast electron transfer capability.[86,87] The PAAm holds a high permeability, and a hydrophilic property due to the three-dimensional network structure.[88] In particular, it has been used to effectively immobilize biomolecules while maintaining their reactivity.[89] The hydrogel is also anti-fouling and can prevent non-specific adsorption of non-target molecules on the surface of a sensor.[90] Furthermore, to the best of our knowledge, a high-performance bioelectronic tongue integrating hydrogels with umami receptors for sensitive monitoring of umami substances has not been demonstrated.

In this study, the T1R1 VFT produced from *E. coli* was used for analysis and practical application to evaluate umami taste. The taste ligand efficacy of T1R1 VFT to investigate umami taste ligands and their synergistic effects was measured using tryptophan fluorescence quenching assay. Moreover, hydrogel-based bionic electronic tongue was developed for the highly sensitive detection of umami

substances in fish extract samples. T1R1 VFT was selectively immobilized on the floating electrode of a CNT-FET using a cysteine linker. Then, a protective membrane layer was formed by physically adhering a PAAm conducting hydrogel film to the surface of a CNT channel region. Umami substances and fish extract samples were tested using the hydrogel-based bioelectronic tongue.

6.2 Taste ligand efficacy analysis in ligand binding domain of human umami taste receptor using a tryptophan fluorescence assay

The functionality of prepared T1R1 VFT for MSG and IMP was evaluated using a tryptophan fluorescence quenching assay (**Figure 6.1**). Tryptophan residues in a protein exhibited intrinsic fluorescence at emission wavelengths around 350 nm. After adding various concentrations of umami solutions to T1R1 VFT solutions, data of fluorescence intensity changes were normalized by the original fluorescence intensity to estimate the relative fluorescence intensity $\Delta F/F_0$. The binding of ligands to receptors led to the conformational changes of the receptors, which could quench the fluorescence intensity.[91] In this work, the binding of umami substances to T1R1 VFT induced conformational changes in the protein, which resulted in fluorescence quenching of the tryptophan residues. As the concentrations of MSG and IMP increased, the relative fluorescence intensity also increased. The results indicated that the T1R1 VFT was refolded while maintaining its functionality.

Figure 6.2 shows the tryptophan fluorescence quenching assay results toward various tastants. The changes of relative fluorescence intensity reached almost 6 % when umami tastants of MSG and IMP were introduced. However, the relative fluorescence intensity changes were less than 2.3 % by the addition of non-umami tastants such as sodium chloride (NaCl, salty tastant), quinine (bitter tastant), citric acid (sour tastant), and sucrose (sweet tastant). The results indicated that the prepared T1R1 VFT protein could discriminate umami substances from other non-umami tastants.

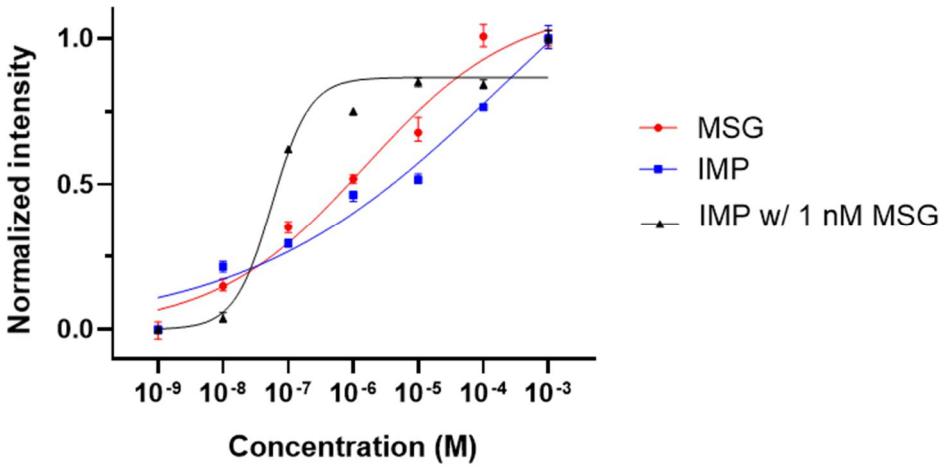

Figure 6.1 Dose-dependent responses of T1R1 VFT to umami taste molecules and their synergistic effects using tryptophan fluorescence quenching assay

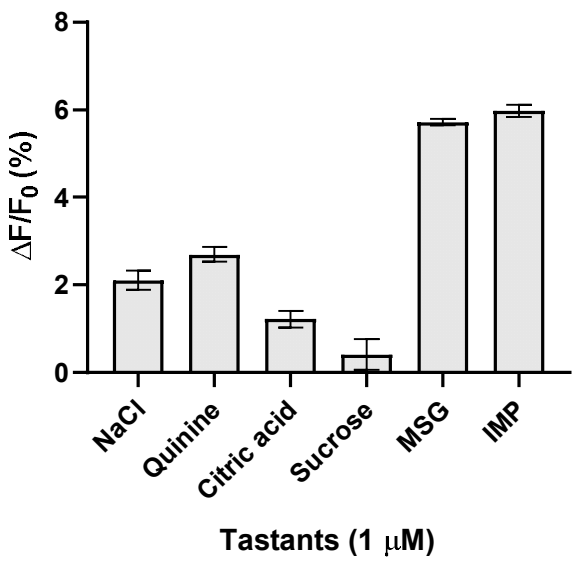

Figure 6.2 Selective responses of T1R1 VFT to umami taste molecule using tryptophan fluorescence quenching assay

6.3 Fabrication of hydrogel-mediated CNT-FET using T1R1 VFT

Figure 6.3 shows the schematic diagram of a hydrogel-based bioelectronic tongue using the T1R1-VFT. The scanning electron microscopy image of the channel region in the CNT-FET is shown in Figure 6.1a. Briefly, a CNT channel region was patterned on a SiO_2 substrate using conventional photolithography, and a CNT solution was dropped on the channel region of the patterned substrate for selective adsorption. Then, source, drain, and floating electrodes were fabricated via photolithography and thermal evaporation methods. Afterward, the floating electrodes of the device were functionalized with cysteine linkers, and a recognition element, T1R1 VFT, was selectively immobilized on the floating electrodes of the CNT-FET via amide bonds. Finally, a hydrogel solution was dropped on the surface of the channel region. The formed hydrogel layer could provide a stable hydrophilic environment to maintain the activity of receptors. Current-voltage (*I-V*) curves show prepared hydrogel-based bioelectronic tongue had good electrical characteristics after introducing T1R1 VFT and hydrogels (**Figure 6.4**). Umami substances comprised of rather small molecules in the sample solution could spread into a hydrogel film and bind to the T1R1-VFT on the floating electrodes of the CNT-FET. The binding of umami substances to the T1R1 VFT resulted in conductance change of the underlying CNT channel, which allowed sensitive detection of umami substances in real time.[62] However, the hydrogel film blocked the relatively large molecules such as proteins and cells from the surface of CNT-FET, minimizing a possible contamination due to non-specific adsorption on the sensor surface. Therefore, the hydrogel-based bioelectronic tongue was expected to have a high sensitivity and a stability over a long term period for the detection of umami substances.

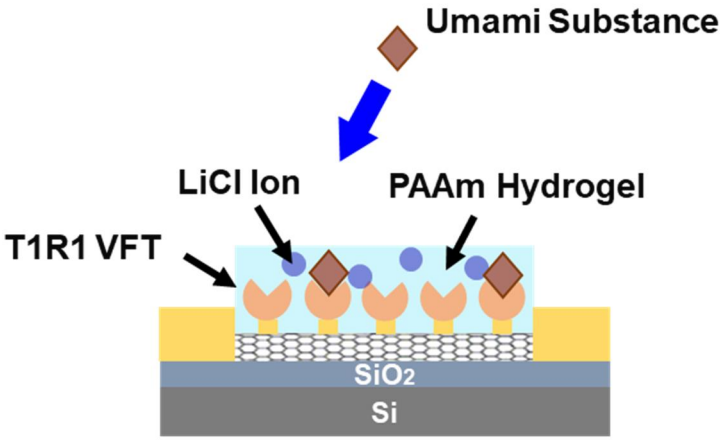

Figure 6.3 Schematic illustrations of a hydrogel-based bioelectronic tongue using the T1R1 VFT

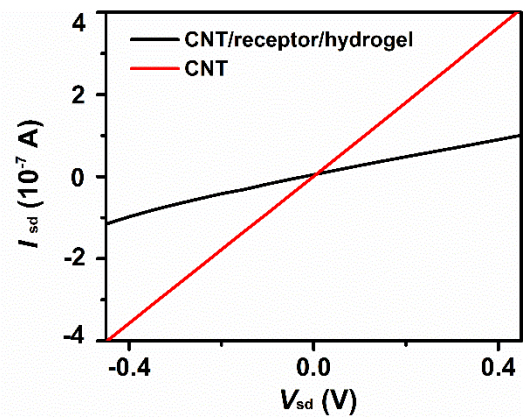

Figure 6.4 *I-V* curves of a sensor before and after the modification of receptor and hydrogel

6.4 Real-time and selective responses to umami tastants

Figure 6.5 depicts the real-time response of a hydrogel-based bioelectronic tongue to IMP solution with different concentrations. The source-drain current of a sensor was monitored in real-time after the introduction of umami solutions to the sensor. A constant bias voltage of 0.1 V was maintained during the measurements. Note that, when a series of solutions were introduced sequentially from low to high concentrations, the current immediately increased and then was stabilized to a fixed value. Importantly, the sensor began to show a response to the addition of a 1 fM MSG and IMP solution. These results indicate a 10 times lower detection limit compared with previous sensors based on T1R1 VFT.[46,62,92] Such a high sensitivity can be attributed partly to the hydrogel coating which could have enhanced the stability and reliability of our sensors. Note that previous sensors for umami tastants usually exhibited a saturated sensor signal at a much lower concentration, which limits the range of detection and cannot truly mimic a human taste sensation (**Table 6.1**). Our sensors could detect IMP and MSG over a wide range of concentrations covering human umami taste thresholds. These results show that our sensor had a high sensitivity and a wide detection range for umami substances detection.

Figure 6.6 shows the real-time response of a sensor to various taste substances. The source-drain current was measured while 1 μM of non-umami tastants and 1 nM of umami tastants were sequentially added to the sensor. Note that there were negligible current changes caused by non-umami tastants with a relatively high concentration, while the current changes significantly increased by the introduction of MSG and IMP solutions. Such a selective response of our sensors can be contributed to the high binding capacity of T1R1 VFT for umami tastants.[85] The result indicated that the bioelectronic tongue could discriminate umami tastants from

other tastants with high selectivity.

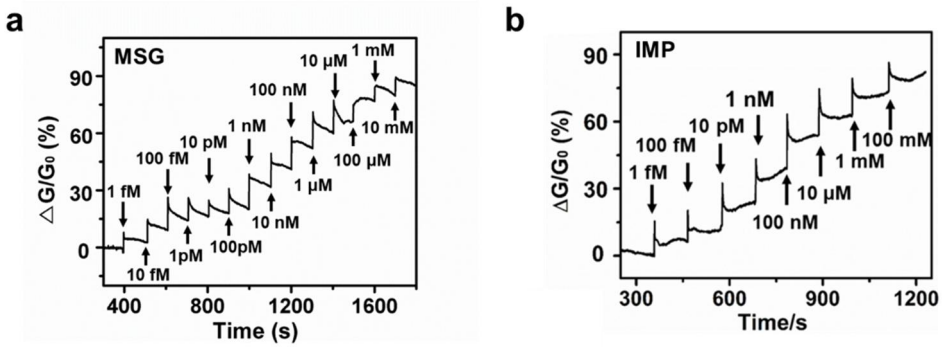

Figure 6.5 Real-time response of a hydrogel-based bioelectronic tongue using the T1R1 VFT to umami tastants

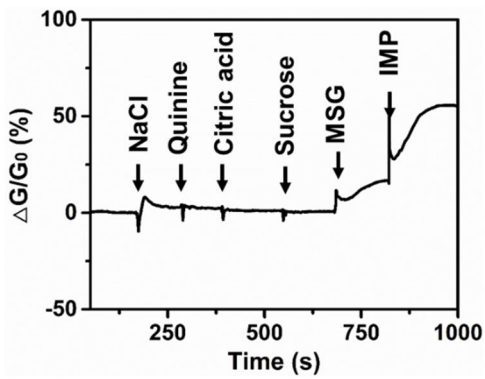

Figure 6.6 Selective responses of a hydrogel-based bioelectronic tongue using the T1R1-VFT to umami tastants

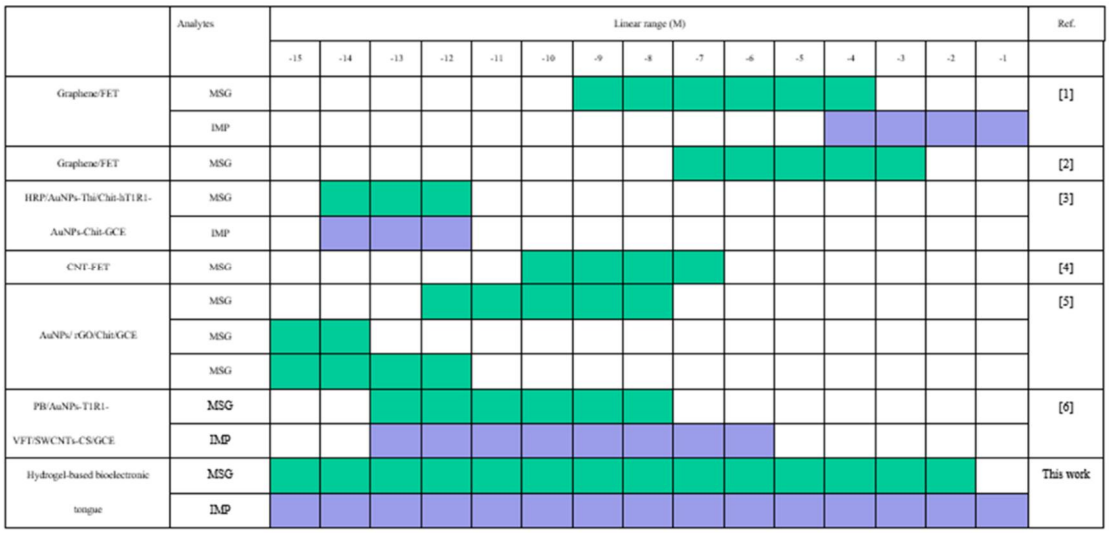

Table 6.1 Analytical performance of the various bioelectronic tongues for umami substance detection

6.5 Measurements of fish extract samples using hydrogel-mediated CNT-FET using T1R1 VFT

Figure 6.7 depicts the fluorescence quenching response of the receptors to different concentrations of fish samples. As the diluted concentrations of fish samples increased, the fluorescence quenching signal increased. These results demonstrated the ability of the receptors to specifically bind umami compounds in fish samples.

To test the applicability of the hydrogel-based bioelectronic tongue in real samples, it was utilized to evaluate the umami intensity in fish samples (

Figure 6.8).

Figure 6.8a shows the normalized dose-dependent responses of the sensor to diluted fish samples. Detailed procedures for preparing fish samples are presented in the Materials and method. In brief, 0.5 g/L of fish samples were prepared in HEPES buffer solutions, filtered by ultrafiltration membranes, and diluted to different concentrations in 10-fold volume ratios for sensing measurements. IMP and MSG, the two most dominant umami substances in fish samples, were present at a total concentration of approximately 2×10^{-3} M. The conductance changes of the sensor were measured while adding various concentrations of diluted fish samples to the sensor. The normalized signals were obtained with respect to their maximum values. The sensor began to show a response from the diluted concentration of 10^{-16} (v/v), and the responses were saturated at around 10^{-2} (v/v). The results indicated that the selective binding of the T1R1 VFT and umami substances in fish samples induced responses in our senor. The EC_{50} value of the sensor was calculated by fitting the data using the Hill equation. The volume concentration corresponding to the EC50

value was estimated to be 4.2×10^{-11} (v/v). Using the estimated IMP and MSG concentrations in the fish samples, the measured EC_{50} value by a volume ratio can be converted into a molar concentration of 8.2×10^{-13} M, which is lower than that of MSG and IMP. Presumably, it is due to the synergistic effect of multiple umami substances in fish samples. These results showed that our sensor can detect a trace amount of umami substances in complex environments such as fish samples and can be used for the evaluation of real samples.

Figure 6.8b shows the normalized signals of the sensor to fish samples after different periods of fermentation. Raw fish fillets were stored at 4 ℃ in a refrigerator for 7 days. Fish samples were prepared every day and diluted at 1: 106 in a HEPES buffer solution for use. Sensor responses to fish samples were quantified using the absolute values of the relative conductance change $|\triangle G/G0|$, where G0 and ΔG represent the sensor conductance before the introduction of fish samples and the conductance change after the addition of fish samples, respectively. In the early stage of fish storage, the sensor signals increased slowly, indicating the increase of umami substances in the fish sample. However, after 4 days of the storage, the signals began to decrease significantly. Presumably, after the death of a fish, the ATP in the fish tissue was continuously metabolized and degraded to produce umami substances such as IMP.[93] At the same time, proteins in the fish were degraded by the action of endogenous enzymes, producing umami amino acids such as glutamic acid. Eventually, the umami taste of fish reached its highest level within 4 days, which can be the best period for a fish consumption. As the storage period extended the 4 days, the IMP in the fish was expected to be broken down into hypoxanthine by inosinoidase enzyme, and the umami amino acids were consumed by the multiplying

microorganisms as reported previously.[94,95] Therefore, the umami tastes declined sharply due to spoilage and deterioration of the fish sample. It is noteworthy that our results were in good agreement with previous works about the changes of umami substances in fish under refrigeration.[96] These results clearly show that our sensors were suitable to assess the umami intensity in real samples such as a fish fermented in refrigeration conditions.

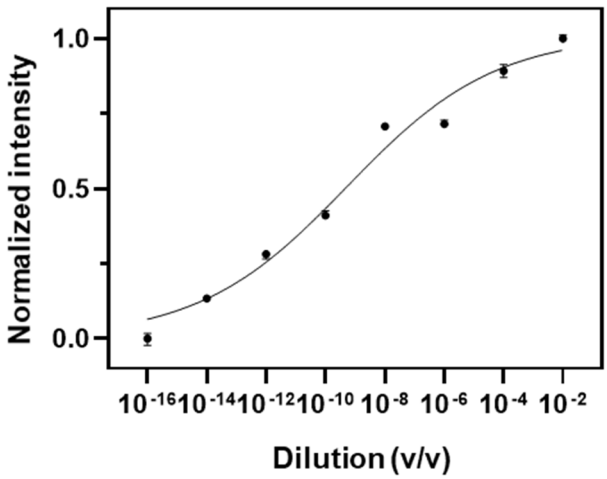

Figure 6.7 Dose-dependent response of the T1R1 VFT to fish extract samples using tryptophan fluorescence quenching assay

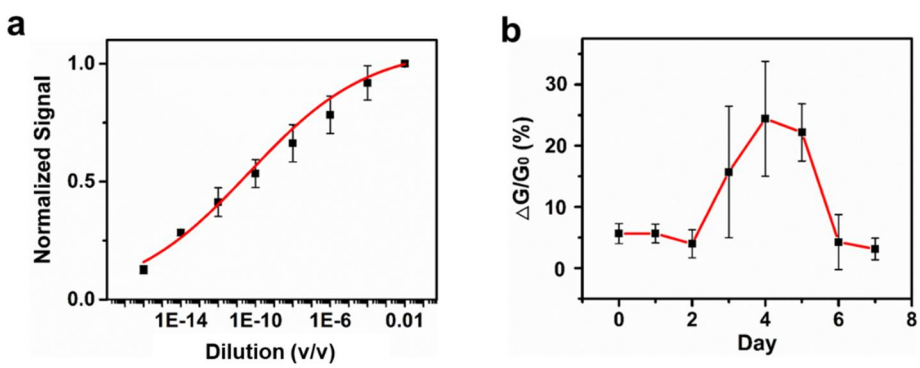

Figure 6.8 Responses of T1R1 VFT-based bioelectronics tongue FET to fish extract samples

(a) Responses of the sensor to various concentrations of umami substances in fish samples (b) Relative conductance changes of the sensor by the addition of fish samples during storage (0-7 days)

6.6 Conclusions

The ligand-binding domain of the human umami taste receptor was produced from *E. coli*, and various analyses and applications involving it were investigated. The efficacy of umami taste substances and their synergistic effects were evaluated using tryptophan fluorescence analysis, which provided a relatively simple way to evaluate umami taste using ligand-binding domains of human umami receptors. The umami taste ligand efficacy analysis using a tryptophan assay could demonstrate the human-like responses.

A high-performance bioelectronic tongue was successfully developed by combining a conductive polymer hydrogel with a floating electrode-based CNT-FET hybridized with receptors. The receptors fused in the hydrogel-mediated nanostructures had a great affinity with umami substances in the defined FET microenvironment, which enabled a highly sensitive and selective detection of umami substances down to 1 fM. Moreover, the device achieved a wide dynamic range of 10^{-15} ~ 10^{-1} for umami detection, which covers the human taste threshold. Also, the sensor could evaluate umami intensities in fish samples. For the detection of large molecules such as peptides, the microstructure of a hydrogel can be controlled by adjusting the ratio of the hydrogel monomers to crosslinkers or adding inactive pore agents. This strategy could be used in other electronic devices to enhance the performance and application of the sensor under physiological conditions.

Chapter 7

Production and functional reconstitution of human photoreceptors

7.1 Introduction

Rod cells and cone cells are the two types of light-sensitive cells existing in the human photoreceptor layer. There are four types of photoreceptors among these cells: rhodopsin (Rho) in rod cells that separates light from dark, and three cone opsins (SW, MW, LW) in cone cells that identify colors. The four photoreceptors absorb light in various wavelengths. The outer segment of the photoreceptor consists of several discs, and light-sensitive opsin exists in the membrane of the disc. Cone opsin and rhodopsin share a similar mechanism, and in vivo, opsin is coupled to 11-*cis*-retinal, a vitamin A derivative, where it exhibits an inactive configuration. In the presence of light, the 11-*cis*-retinal molecule transforms into an all-trans-retinal and is freed from opsin. At the same time, Opsin undergoes a structural conformational change that triggers off a chain of reactions that leads to signal transduction.

Proteins reconstituted using ND are highly stable, compared to other reconstituted proteins.[3] In particular, ND technology is known to be suitable for restructuring GPCRs. The ND consists of a receptor protein, a phospholipid bilayer, and MSP, which encloses the receptor-phospholipid complex which acts as a belt. ND technology can mimic the structure of membrane proteins in nature.

In this chapter, four human photoreceptors were expressed and purified from *E. coli*. Using NDs, the purified photoreceptors were reconstituted, and the physical properties were measured to ensure that the photoreceptors were assembled properly. Moreover, human photoreceptors were expressed and produced in mammalian cells to further confirm their functional signaling. In particular, photoreceptor-expressing viruses were produced using recombinant lentivirus system. Both photoreceptors were produced from *E. coli* and mammalian cell and will be applied to investigate a novel photosensitive biological system with spectral sensitivity as well as vision restoration.

7.2 Expression and purification of photoreceptors in *E. coli* system

Human photoreceptors were expressed as in an insoluble form in *E. coli*. As a result, SDS sulfactant was used to solubilize the insoluble protein prior to purification. Using the 6x His-tag gene was included in the C-terminal polycloning site of the pET-DEST42 vector into which the human photoreceptor gene was inserted, column purification was performed using fast protein liquid chromatography (FPLC). The photoreceptor proteins were successfully purified as shown in **Figure 7.1**. Purified photoreceptors were confirmed by SDS-PAGE analysis (**Figure 7.1a**). The expected band size of at 38.7 kDa for Rho, 40.4 kDa for LW, 39 kDa for SW, and 40.4 kDa for MW was observed, which correlates to the molecular weight estimated by the online ExPASy bioinformatics tool. Moreover, the FPLC results show a single sharp peak (**Figure 7.1b**). The results indicate the photoreceptors were successfully expressed and purified from *E. coli*.

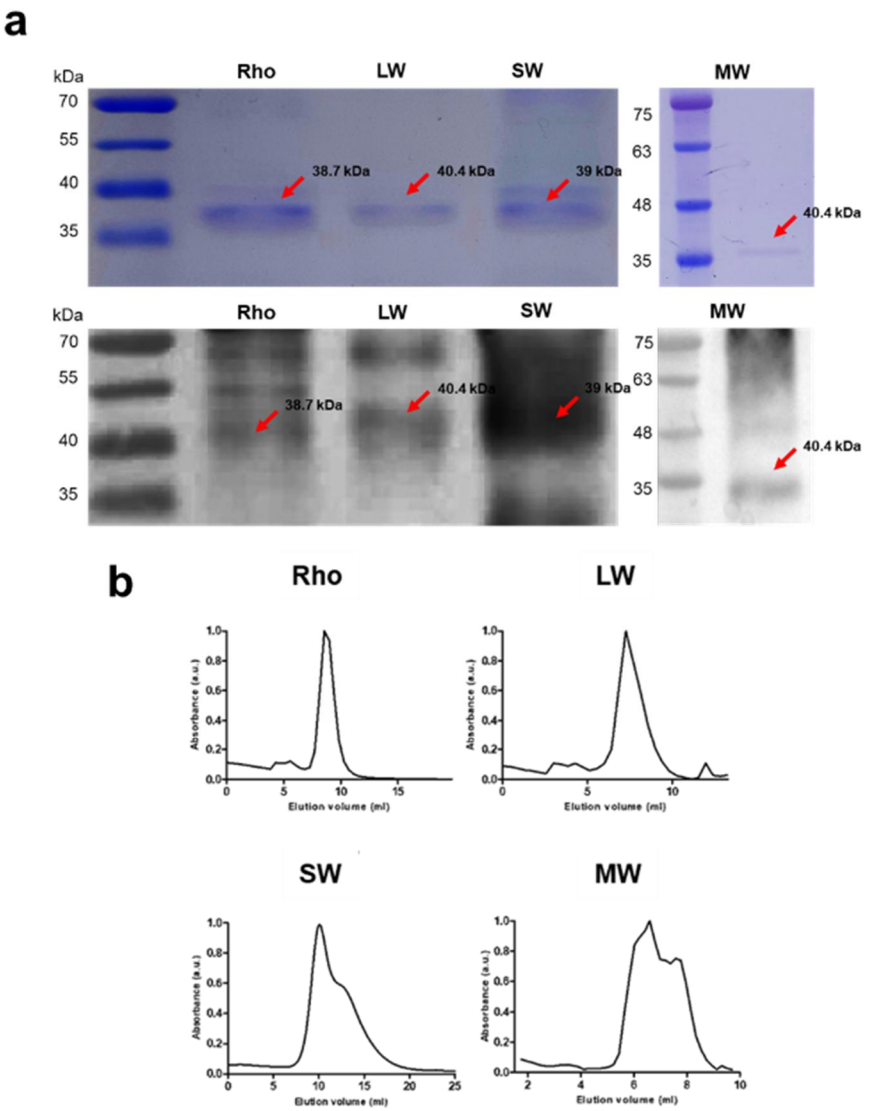

Figure 7.1 Expression and purification of human photoreceptors

7.3 Structural and functional characterization of photoreceptor NDs

Since the purified photoreceptor has a linear structure in a solubilized state, it requires reconstitution to its original folded structure to its original folded structure to function biologically. Human photoreceptors, phospholipid, and MSP1E3D1, which are three components of the ND, were mixed using ND technology, and the surfactant was removed using Bio-Bead.

MSP, one of the ND components, was produced from *E. coli*, and confirmed using SDS-PAGE analysis (**Figure 7.2**). MSP with His-tag indicates the MSP produced using pMSP1E3D1 bacterial expression vector containing 6x His-tag. MSP indicates the MSP produced and His-tag cleaved with further process. His-tagged MSP had a band of 32.7 kDa, while MSP had a lower band of 30 kDa.

Photoreceptors were mixed with phospholipids and MSP for reconstitution. The photoreceptor NDs were obtained from the mixed ND solution through size exclusion chromatography (SEC) (**Figure 7.3b**). The composition of the four photoreceptors in the NDs was confirmed using SDS-PAGE analysis (**Figure 7.3a**). Rho, LW, SW, and MW bands were observed at approximately 40 kDa, and the MSP1E3D1 band was observed at approximately 30 kDa.

The size distribution and homogeneity of the photoreceptor NDs were analyzed using DLS. The average diameters of Rho, LW, SW, and MW NDs were 15.9 nm, 18.4 nm, 15 nm, and 11.7 nm respectively (**Figure 7.4**). In addition, the FE-SEM images clearly showed that the shape of the photoreceptor Rho and SW NDs had a discoidal disc shape (**Figure 7.5**). These results indicate that the NDs were successfully assembled into homogeneous discoidal shapes of proper size.

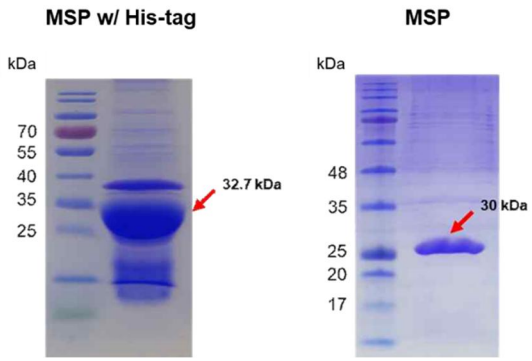

Figure 7.2 SDS-PAGE analysis of MSP with His-tag and MSP

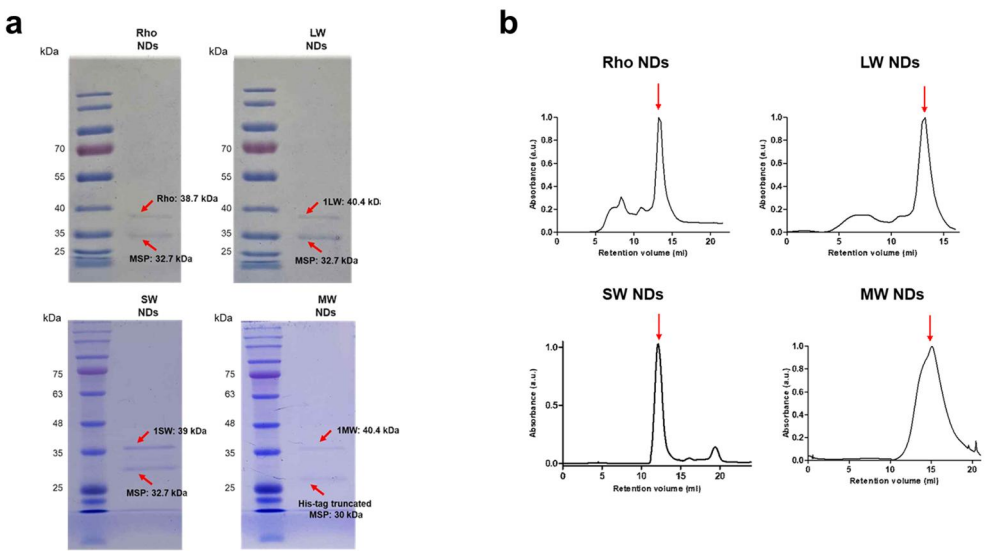

Figure 7.3 Production of photoreceptor NDs

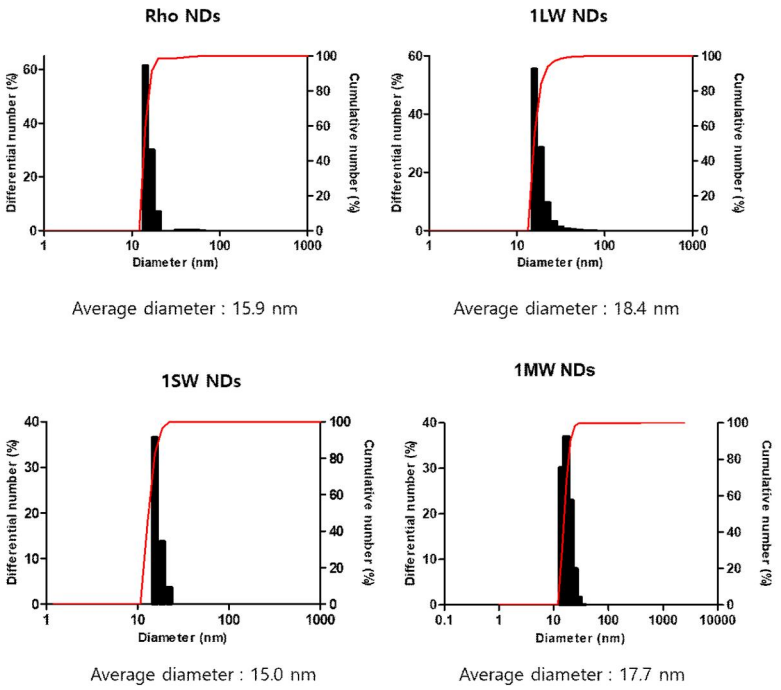

Figure 7.4 Dynamic light scattering (DLS) measurement of photoreceptor NDs

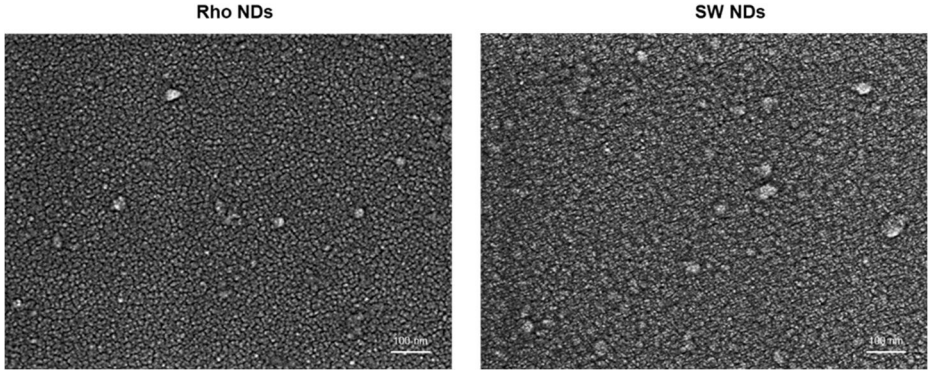

Figure 7.5 Field-emission scanning electron microscopy (FE- SEM) image of photoreceptor NDs

7.4 Expression and production of human photoreceptors in mammalian cell

To confirm the expression in mammalian cells, photoreceptors were expressed in HEK-293 and R28 cells. R28 retinal precursor cells is a cells derived from 6-day-old rats, which are commonly used in retinal cell research. Rho-GFP and LW-DsRED were expressed in both HEK293 and R28 cells (**Figure 7.6**). The fluorescence of the fusion protein, GFP and DsRed, was observed in the location of the cell. Although R28 showed a lower gene expression efficiency compared to photoreceptor-expressing HEK-293 cells. These results indicate photoreceptors can be successfully expressed in retinal precursor cells, R28 cells, and the commonly used HEK-293 cells.

Rho and SW were cloned into lentiviral vectors, which can efficiently deliver the gene of interest and increase the efficiency of expression. The lentiviral cloning map of photoreceptors inserted into the lentiviral vector is shown in **Figure 7.7a**. Rho and SW were successfully cloned to the lentiviral vector and confirmed using electrophoresis analysis (**Figure 7.7b**). The photoreceptor-expressing virus was generated and used to construct HEK-293 and R28 stable cell lines expressing photoreceptors as well as transduce primary neuronal cells expressing photoreceptors for further research. In **Figure 7.8**, fluorescence activated cell sorting (FACS) was performed to sort the cells expressing photoreceptors using the fusion fluorescence protein, RFP. The red-boxed area was sorted and cultured to generate a cell line that stably expressed photoreceptors. The constructed HEK-293 and R28 stable cell line expressing photoreceptors were confirmed using fluorescent imaging (**Figure 7.9**). Red fluorescence was visible in photoreceptor-expressing cells but not in control cells with no expression.

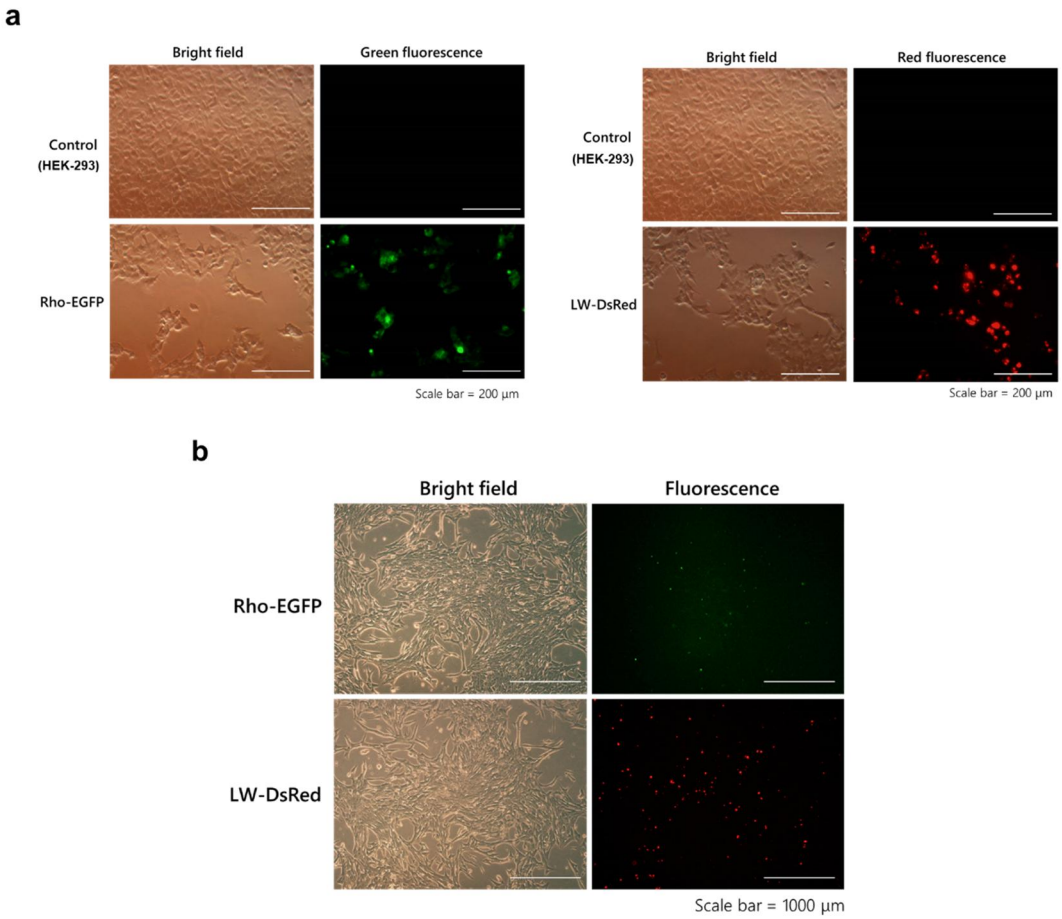

Figure 7.6 Fluorescence images of (a) HEK-293 and (b) R28 cells expressing human photoreceptors

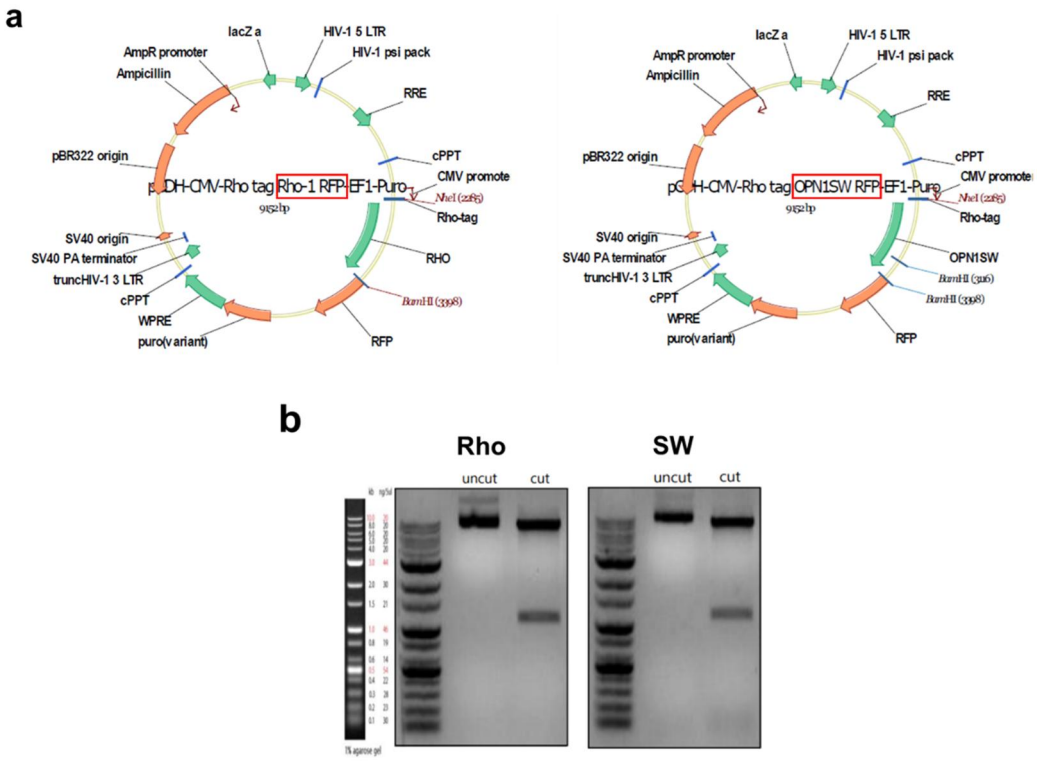

Figure 7.7 Lentiviral cloning for human photoreceptors

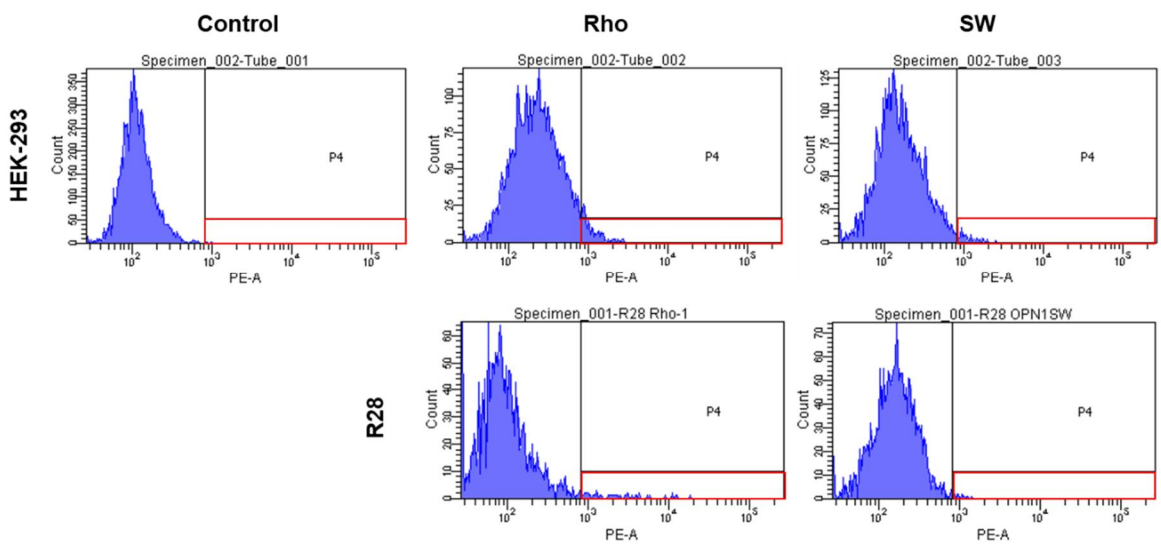

Figure 7.8 Fluorescence activated cell sorting (FACS) of cells expressing photoreceptors

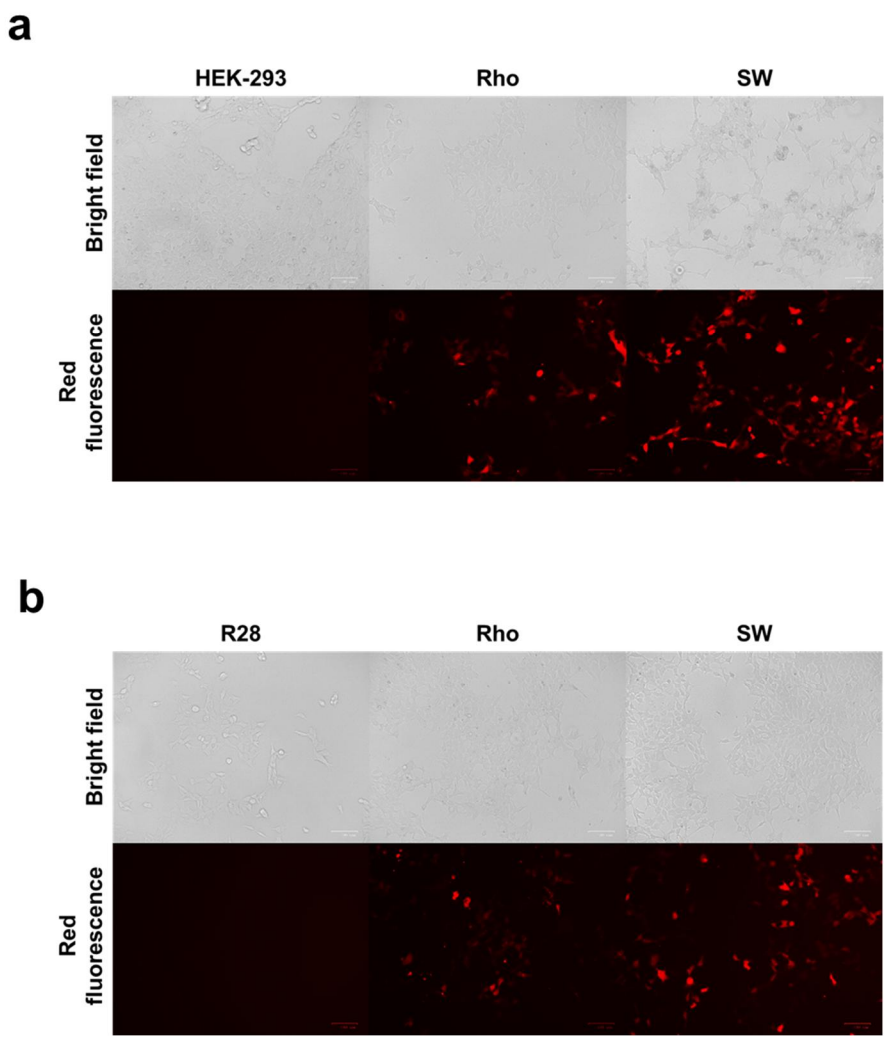

Figure 7.9 Photoreceptor-expressing stable cell line using recombinant lentivirus system

7.5 Conclusions

Herein, photoreceptors were expressed and purified in both *E. coli* and mammalian cells for further analysis and applications. Using the *E. coli* expression system, all four photoreceptors were produced and reconstituted into NDs. The size and morphology of the photoreceptor NDs were confirmed. This photoreceptor NDs can be a useful tool to better understand the physiological and biochemical mechanisms that occur in human visual receptors. Furthermore, it is expected to contribute to the development of technologies to supplement or replace damaged retinas, such as artificial retinas, based on the understanding.

Chapter 8

Human photoreceptors: Analyses and applications to measure optical properties

8.1 Introduction

The retina is a nerve tissue that lines the inside of the eye. When light enters the human eye, the photoreceptor layer of the retina absorbs it, converts it into a bioelectric signal, and transmits it via the optic nerve to the cerebrum's visual cortex. Once damaged, the retina of mammals, including humans, cannot regenerate, and no treatment method, including drugs or surgery, is currently available. Retinal pigmentosa (retinis pigmentosa, RP) and degenerative macular degeneration (age-related macular degeneration, AMD) are two diseases caused by damage to the retina's photoreceptor layer. These diseases have a significant negative impact on quality of life, affecting 30% of the total visually impaired population. These diseases have a significant impact on the quality of life of individuals, as well as the social and economic costs of protecting and supporting them on a national scale, as work force is lost due to visual impairment. As a result, a technology that can supplement or replace the lost function of the retina, such as the development of an artificial retina, is required. The first step should be to understand the physiological and biochemical mechanisms that occur in actual human visual receptors. Therefore, the analysis and application of artificial photoreceptors could aid understanding and enable one step forward in the development of vision restoration technology.

In this study, photoreceptors produced from E. coli and mammalian cells were used to analyze the photo-sensitive function and optical properties. SW and Rho NDs was used to examine the optical features and a novel optical waveguide with refractive index modulation of artificial photoreceptor NDs was designed for all-optical switching and signal processing applications as well as medical applications including, as reported, vision restoration cure-studies using other NDs.[97,98]

Using the human photoreceptors produced from mammalian cells, the retinal-binding function was analyzed and a SW and Rho-expressing neural spheroid was

generated to play the role of an eye via lentivirus transduction. These photosensitive spheroids were used in two types of devices: those with intact dissociated neurons and those with intact neural spheroids. In the micro-devices, the photosensitive spheroids connected with neural networks on cell body and axons. Signal transmission to adjacent neural networks was measured using a photosensitive spheroid stimulated by photo-stimulation.

8.2 Analyses and applications to measure optical properties using photoreceptors produced in *E. coli*

8.2.1 Functional characterization of photoreceptor NDs using tryptophan fluorescence assay

Figure 8.1 shows the structural and functional transformation of the Rho, LW, and SW NDs as a result of their interaction with the 11-*cis*-retinal molecule. Empty NDs without receptors were used as a negative control, and the change in tryptophan fluorescence intensity was measured after the addition of 10 μM의 11-*cis*-retinal. The relative fluorescence intensity was calculated with the formula $\Delta F/F_0$ (%) = $[(F_0 - F)/F_0] \times 100$. F_0 and F refer to the fluorescence intensity of the receptor before and after the treatment of ligand molecules, respectively. The Rho, LW, and SW NDs all demonstrated significant differences in fluorescence intensity when compared to empty NDs. As a result, it is assumed that the photoreceptor NDs, when bound with the 11-*cis*-retinal, caused a conformational change. These findings demonstrate that the produced photoreceptor NDs have functionality by interacting with 11-*cis*-retinal, which is required for light signal transduction. When the light of various wavelengths absorbed by the photoreceptor is given in a state where the photoreceptor ND and 11-*cis*-retinal are combined in an additional experiment, the 11-*cis*-retinal structure changes to an all-trans form.

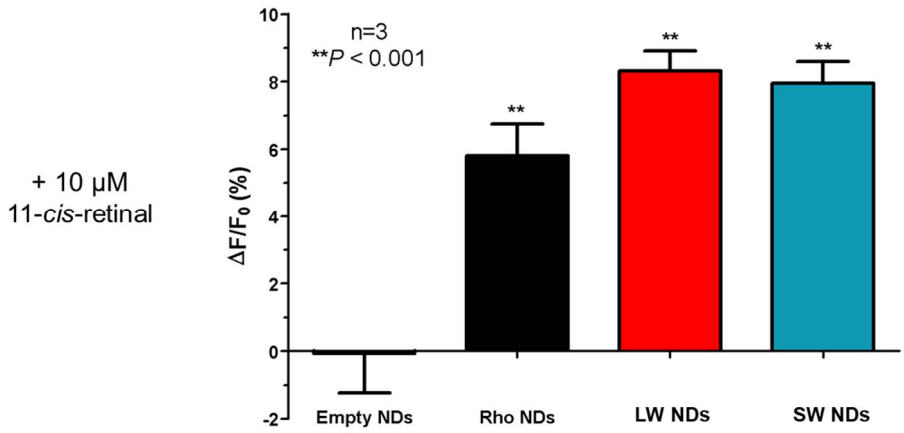

Figure 8.1 Characterization of photoreceptor NDs using tryptophan fluorescence quenching assay

8.2.2 Refractive index measurement of photoreceptor NDs

As one of the main optical characteristics for beam propagation in materials, the refractive indices were investigated by a refractometer designed by Nemoto,[99] as described in **Figure 8.2** with the equation for calculating the refractive index from beam shift and incident angle. Using white light from a supercontinuum source, which emitted collimated beam like a laser without isotropic emission, we made several filtered beams with specific wavelengths (**Figure 8.2a and 8.2b**). SW- and Rho-NDs showed different refractive index characteristics, as shown in **Figure 8.2**. Upon exposure to beam wavelengths in the visible range, the SW-NDs exhibit a stable refractive index of approximately 1.334, whereas the Rho-NDs refractive indices fluctuate between 1.281 and 1.348 (**Figure 8.2c**). The refractive index of the modeled cone photoreceptors was estimated before to range from 1.340 to 1.394 based on a method using reflected light;[100] these estimations match our SW-ND results well. The variations in refractive index could come from differences in light absorption according to the spectral characteristics of seven different wavelength beams (**Figure 8.2b**).

To examine the response of retinal addition and photoactivation, the variation of the refractive indices is described in **Figure 8.2d-f**. The optical setup was designed based on the samples' spectral sensitivity; the LED lights emitting at 410 and 490 nm for the stimulation were chosen on the basis the sensitive wavelengths of SW- and Rho-NDs, as studied in previous work,[101] and a 635 nm wavelength red laser was used to avoid interferences from reactions in samples (**Figure 8.2d**). According to the refractive index, the beam refracted through several interfaces when transmitting from the cuvette to the sample. The refracted angles are illustrated in **Figure 8.2e**; the refraction angle is determined under Snell's law at the interfaces

between different materials. Because all waveguiding experiments are performed with the incident beam under 95 mW, photothermal damage does not exist because incident beam is barely absorbed by transparent liquid.

The refractive indices of both SW- and Rho-NDs were lowered by adding 11-*cis*-retinal but then increased at the end of the experiment (**Figure 8.2f**). First, benzene-based solvent for retinal, which has an n_0 of over 1.7, could assisted in increasing the refractive index of the sample solution when blended with the NDs in HEPES buffer. After evaporation of 1% (v/v) benzene solvent with a very small quantity related to the whole medium, the samples showed steady results, even though benzene has an unstable evaporation rate.[102,103] Photoactivation and photobleaching could lead to variations in n_0 of the mixed sample solution after retinal addition. The combination of the change in protein structure with retinal binding to photoreceptors and producing all-*trans*-retinal results in an increase in refractive indices.[104,105] For the origin of refractive index change, several effects were inspected by solvents, that is, biological reactions for sample in solution. With a high refractive index of benzene, the total refractive index was governed by the conformational change of the photoreceptors in the NDs, which was triggered by phototransduction with 11-*cis*-retinal. Furthermore, the solvent plays an important role in determining the refractive index of samples with solvent accessibility, which affects the protein's folding and retinal molecule stability (**Figure 8.2f and 8,2h**).[106] Benzene amplified the refractive-index modulation to be over 1.7, which is relatively higher than that of HEPES buffer with just 0.0005. In previous works, the change in the refractive index of approximately 0.2 for a tungsten oxide and hydrogen composite, HxWO3, was used for gas sensing via chemical reaction, and mechanical strain was applied to polystyrene silver nanocrescents implanted in PDMS to modulate the refractive index.[107] The variation in the refractive index of our samples

was over 0.18, which is sufficient for use in a new optical device as a waveguide-based optical switch. This outstanding phenomenon involving the change of refractive indices was utilized later with the waveguiding experiment for beam propagation control, **Figure 8.3** and **Figure 8.4**.

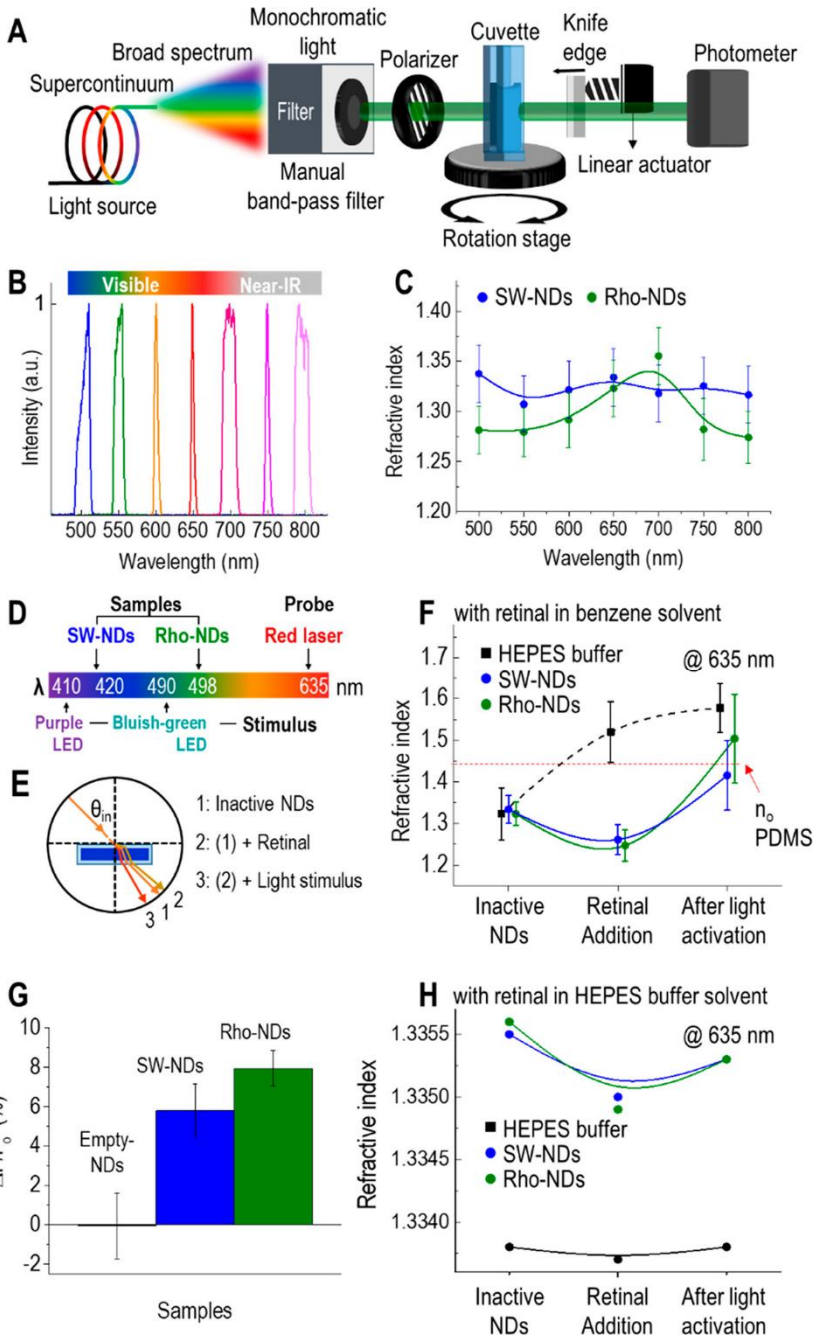

Figure 8.2 Refractive index measurement of photoreceptor NDs

8.2.3 Fabrication of PDMS and photoreceptor ND-filled waveguides

To apply the variable refractive indices of our photoreceptor NDs, we designed simple waveguide as an optical device with our ND samples and a PDMS structure, which was chosen because of its suitable optical properties, chemical stability for liquid sample, and facile fabrication.[108] The photosensitive ND-based waveguide with flexible structure would be applied to various fields including wearable devices as a novel optical material, whereas the usual optical metamaterials with brittle elements such as silicon, Ag, and Au are hardly employed for a flexible device. Using a mold made by 3D printing, the PDMS formed grooves and a guide pattern. By the total reflection of light, which indicates the reflection of most of the light at a specific surface and is governed by the relation of refractive indices between the surrounding materials, the incident beam from 635 nm laser was guided through the PDMS-based waveguide as shown in **Figure 8.3**. The most important factor is that the refractive index of PDMS, 1.43, is in between the refractive indices of our samples. Therefore, according to the refractive index, beam propagation, and waveguiding can be expected, as shown in the schematic of **Figure 8.3**. The relationship among the refractive indices of samples and their conditions determines the beam refraction from light that is highly focused by an objective lens making various incident angles. At the interface, the empty groove and PDMS can reflect most of the light and satisfy the total reflection condition with specific incident angle because the refractive index of PDMS is larger than that of the sample solution. Since the refractive indices of the ND sample varied, the profile of the beam propagation according to the difference in refractive index at the interface was also changed by adding retinal light and photoactivation by light stimulation.

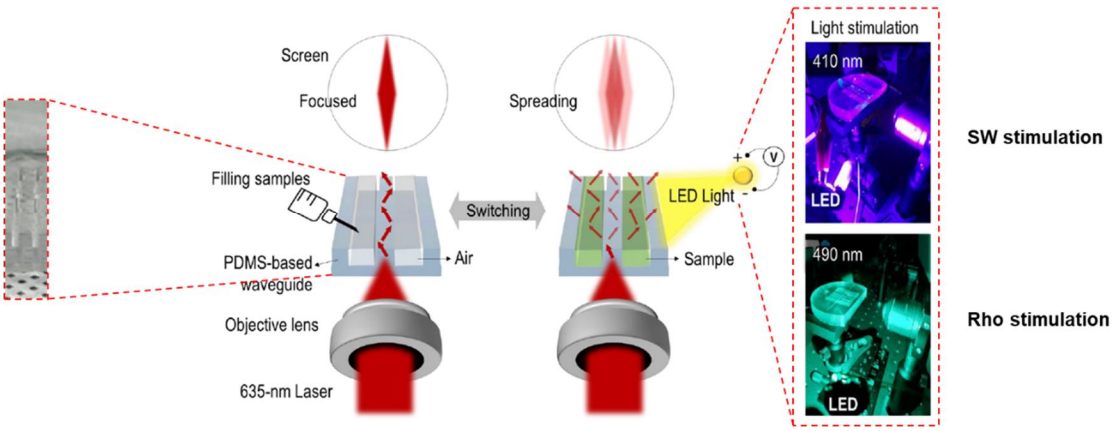

Figure 8.3 Schematic diagram of PDMS and photoreceptor ND filled waveguides

8.2.4 Waveguiding of photoreceptor NDs using PDMS and photoreceptor ND-filled waveguide

To examine the waveguide characteristics as an optical application of photoreceptor-embedded NDs (photo-NDs) with the tunable refractive index, we monitored the light profile projected on screen and the intensity of the guided beam (**Figure 8.4**). Several conditions with the combination of sample types, SW- and Rho-NDs, and stimuli of purple and bluish-green LEDs determine the target wavelength for use in optical switching and signal processing. Generally, under all the conditions beam broadening was observed from the whole profile and row-sectional view (**Figure 8.4a-d**). At the center of the screen, the distribution of collimated light by the waveguide was observed, and then the beam intensity in the detecting area gradually decreased as the beam spread. After retinal addition and photoactivation, the photo-ND-filled waveguide provided a wider beam profile as shown in **Figure 8.4a-d**. These graphs as a row-sectional view exhibit the beam-propagation change by photoactivation effect. Since the incident beam was focused before encountering the waveguide, it has to be highly spread in all directions without any confinement system. Our PDMS-based waveguide led the light to transmit into a narrow gap according to the total reflection with the relation of refractive indices at the interface between PDMS and the empty space containing air. If the relation of refractive indices is reversed by filling and activating our photo-NDs for optical modulation, the incident beam could be spread, losing confinement character. As the refractive index of the photoactivated SW-NDs by 410 nm stimulus approached that of PDMS (n(PDMS) ~ n(SW-NDs)), the beam profile was enlarged and changed slightly with a broad peak by mixing of guided- and transmitted-light under weak total reflection at interface. For Rho-NDs, the incident beam propagated through adjacent waveguides, and two divided beams were clearly projected on the

image screen because the refractive index of the photoactivated Rho-ND by 490 nm stimulus was relatively larger than that of PDMS (n(PDMS) < n(Rho-NDs)) as reversed confinement condition (**Figure 8.4d**). Also, nonphotoactivated samples without proper wavelength stimuli such as SW-NDs under 490 nm LED light and Rho-NDs under 410 nm light provided minor or no expansion in beam profiles as the maintaining higher refractive index of PDMS compared to both photo-NDs (**Figure 8.4b and 8,4c**).

The refractive index changes due to photoactivation gave rise to fluctuations in the projected beam shape and intensity on the screen, which was assigned as the full width at half maximum (FWHM) divided by the maximum intensity (FWHM/Max) parameter. As represented in **Figure 8.4e**, FWHM/Max values were extracted and compared from the images under the different LED wavelengths and for two types of samples. These results were used to investigate the spectral sensitivity and the phase change of the samples. After retinal addition, the SW- and Rho-ND solutions reacted considerably by pump lights at wavelengths of 410 and 490 nm, respectively; the reactions were manifested by expanding the beam width. In the reversed cases, the differences in the response of the stimulating lights at wavelengths of 490 and 410 nm for the SW- and Rho-NDs were small. Accordingly, the FWHM/Max of SW-NDs, with high sensitivity to 410 nm LED light, underwent large changes, and Rho-NDs clearly reacted to 490 nm LED light after photoactivation. This waveguiding modulation resulted in a decline in beam intensity over a specific area on the photodetector. To carefully investigate the duration of the decline, the beam intensity was detected during photoactivation (**Figure 8.4f**). After retinal addition and photoactivation, all samples initially showed a drastic decrease in intensity and slowly returned to their original position over approximately 10 min.

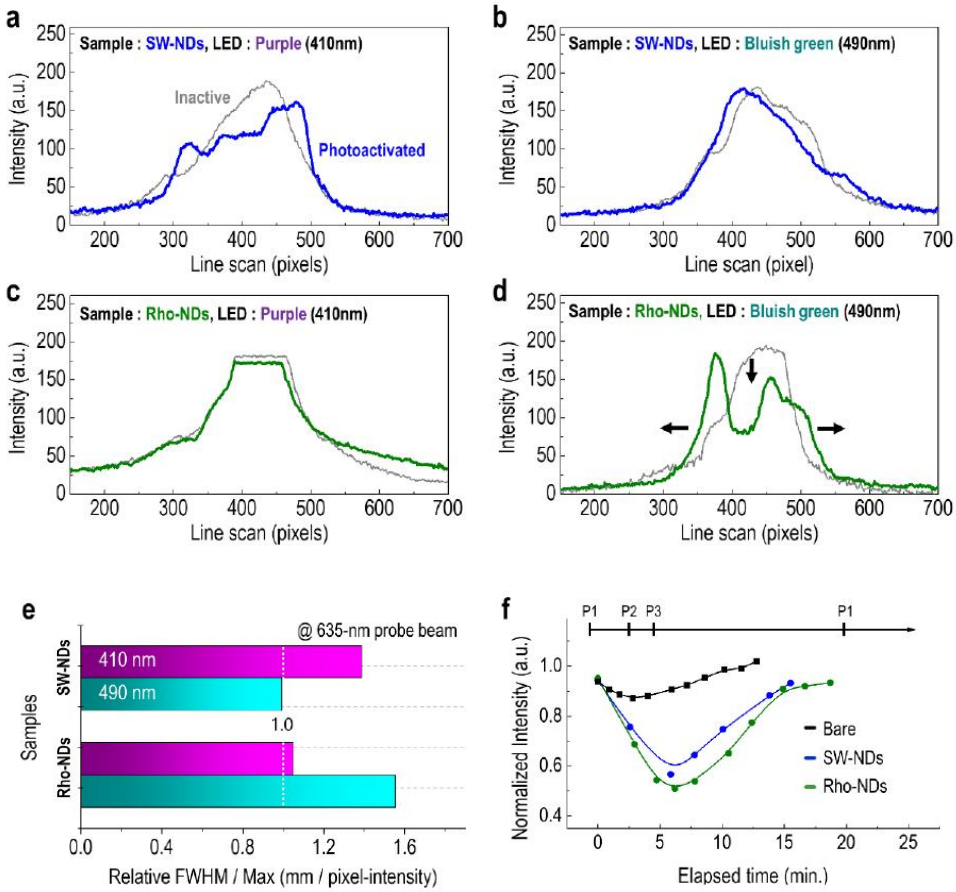

Figure 8.4 Beam profile intensities for photoreceptor NDs

P1: inactive NDs
P2: retinal added NDs
P3: photoactivated NDs

8.3 Analyses and applications to measure optical properties using photoreceptors produced in mammalian cell

8.3.1 Functionality analysis of photoreceptors using calcium assay

For the channel activation test, all four photoreceptors were used. In the presence of 11-cis-retinal, fluorescence signals were recorded from cells expressing all four photoreceptors. However, no significant changes in fluorescence signal were found in control cells with receptor expression, as well as in cells expressing photoreceptors in the absence of 11-cis-retinal. The intensity of green fluorescence was observed in cells expressing all four photoreceptors, indicating that 11-cis-retinal binding and photoactivation resulted in intracellular signal transduction and calcium ion influx.

Figure 8.5 shows the calcium flux assays of HEK-293 cells expressing photoreceptors. For the channel activation test, all four photoreceptors were used. In the presence of 11-*cis*-retinal, fluorescence signals were recorded from cells expressing all four photoreceptors. However, no significant changes in fluorescence signal were found in control cells with receptor expression, as well as in cells expressing photoreceptors in the absence of 11-*cis*-retinal. The intensity of green fluorescence was observed in cells expressing all four photoreceptors, indicating that 11-*cis*-retinal binding and photoactivation resulted in intracellular signal transduction and calcium ion influx.

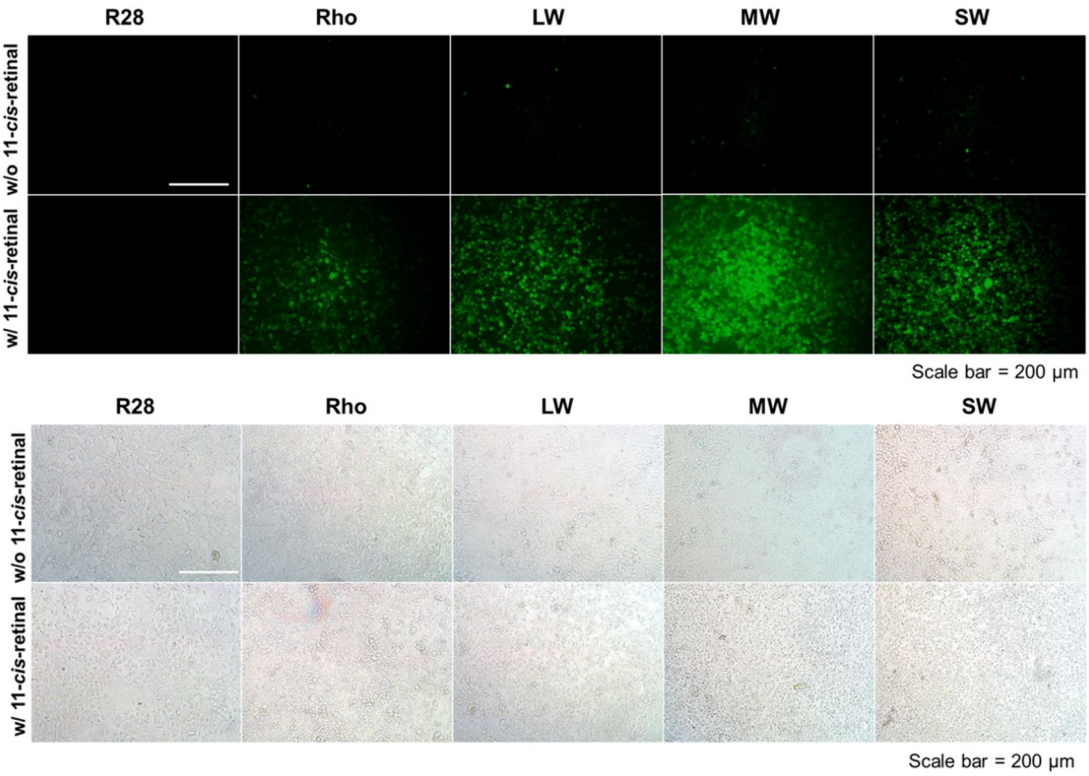

Figure 8.5 Calcium assays of R28 cells expressing photoreceptors

8.3.2 In vitro neural circuit using photoreceptor-expressing neural spheroid

We developed an *in vitro* model of the eye-to-brain circuit integrated with human photoreceptors, such as rhodopsin and opsin. By the photo-stimulation of photoreceptors with specific spectral sensitivity to each type, the retina generates a signal. Through the optic nerve, these signals are transmitted to the brain. In this study, we have demonstrated the features of the visual system, including the generation of signals by photoreceptors, the transmission of signals by axons, and the reception of signals by cortical neurons. This system has two key characteristics; (i) recapitulation of the reaction in a visual system by photo-stimulation through the convergence of artificial human photoreceptors and in vitro neural circuit and (ii) discrimination of colors based on selective responses to specific wavelengths of light, bluish-purple for short-wavelength and green for middle-wavelength.

To construct the *in vitro* model of the eye-to-brain circuit as shown in **Figure 8.6a**, we first loaded primary rat embryo cortical neurons into a spherofilm, an array-type frame for mass production of spheroids. After one week of culture, neurons in the spherofilm formed uniform neurospheroids. After neurospheroids were formed, viral vectors containing human Rho or SW DNA were administered. In neurospheroids, human photoreceptors, such as Rho or SW, were expressed.

The eye-to-brain model in the dumbbell shaped device has two big circle area for two spheroids at the end of edge, and those are connected by the narrow gap in the middle. (**Figure 8.6a**) The calcium ion response for light stimulation on the eye-to-brain model was obtained with the relatively high spike firing rate and low spike intensity, comparing to other measurements. In the immunofluorescent staining images, the axon reached the neurospheroid located on the opposite side. (**Figure 8.6b**) It is expected that the photospheroid signal was transmitted to the intact

neurospheroid after photostimulation. Under the 410 nm wavelength photostimulation, the SW spheroid was stimulated and transmitted to the intact neurospheroid, which captured by the calcium assay fluorescence images. (**Figure 8.6c**)

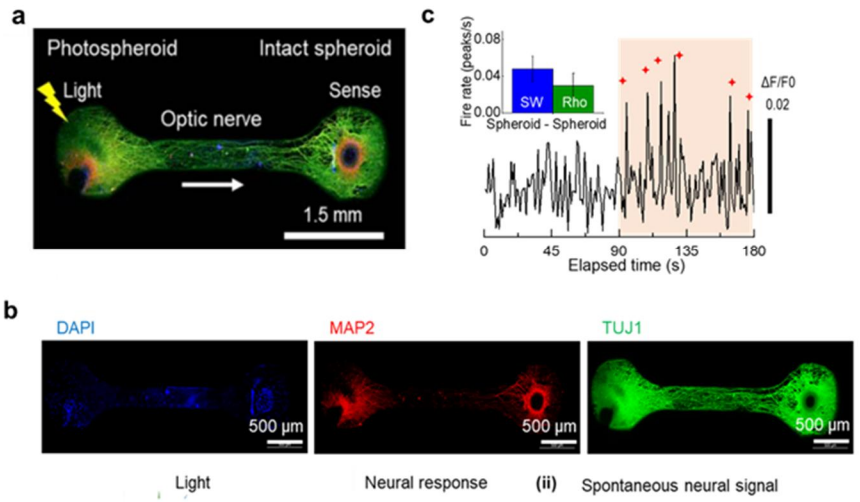

Figure 8.6 3D in vitro visual system with photo- and intact-spheroids

(a) The responses of fluorescence intensity in SW-photospheroid and (inset) the comparison of firing rate (b) Immunofluorescence images of neural connection between the photo and intact spheroid. (DAPI: blue, MAP2: red, and TUJ1: green)

8.4 Conclusions

Although smell and taste require multiple receptor types to recognize a single ligand, only four types of photoreceptors are required to identify the broad spectrum of visible light in vision. Therefore, photoreceptors can be attractive biomaterial for various potential application.

For photoreceptor NDs, not only it can be utilized to target small molecules such as retinal molecules as in the case of many other GPCR NDs but also can recognize the optical properties targeting light. Rho and SW NDs demonstrated exceptional spectrum-dependent sensitivity with human-like characteristics. Several optical measurements revealed exceptional optical characteristics with a refractive index variation greater than 0.18 from the Rho-ND, which is sufficient for optical devices..[109] A light signal was detected as a biological sensory system using an optical property of photo-NDs that allows optical modulation with nanobiomaterial.

Using the virus particles expressing photoreceptors, Rho and SW, an *in vitro* model of the eye-to-brain circuit was developed to transmit signals only in response to light of specific wavelengths. Photosensitive spheroids were successfully mass-produced and transported into a neural circuit *in vitro* without viral contamination. Additionally, photospheroids spontaneously developed axons to the outside, and these axons were connected to intact neurons and neurospheroids. Through these connections, signals generated by the photo-stimulation were transmitted from Photospheroids to the neural network. Based on these results, we suggest that an *in vitro* eye-to-brain model expressing human photoreceptors could provide a potential platform for screening drugs for the treatment of blindness. Furthermore, various types of photospheroids may also be applied to a visual system capable of recognizing input images beyond simple color perception of light.

Chapter 9

Overall discussion and further suggestions

Overall discussion and further suggestions

Measuring the GPCR activity and function is critical in food, environmental, and biomedical applications. Therefore, developing tools for functional GPCR research is critical. GPCR is known to be difficult to express in heterologous cell systems. Therefore, producing and engineering functional GPCRs is critical for developing tools for GPCR research and practical applications in areas such as food, the environment, and biomedicine.

In these theses, the various approach to engineering and producing human taste receptors and visual photoreceptors were performed. For utilizing human sweet and umami taste receptors, a primary ligand-binding domain of the receptor was mass-produced from *E. coli* as an alternative strategy to using a whole receptor, which is difficult to overexpress in *E. coli*. These were analyzed independently with tryptophan fluorescence assay and combined with conducting nanomaterials to evaluate sweet and umami taste in a practical manner. Human photoreceptors NDs produced from *E. coli* and photoreceptor-expressing virus produced from mammalian cells were used to for expected for analysis to better understand the physiological and biochemical mechanisms in human photoreceptors and apply this knowledge to the development of technologies to treat or restore vision.

In chapter 4, a primary ligand-binding domain of a human sweet and umami taste receptor, the T1R2 VFT and T1R1 VFT, were successfully produced from *E. coli* as an alternative strategy to using a whole receptor. The purified T1R2 VFT and T1R1 VFT were successfully expressed and purified with high yield and purity. To restore their original function, the purified samples were refolded. The functions were tested using a tryptophan fluorescence assay, and both T1R2 VFT and T1R1 VFT responded to their representative tastants, sucrose and MSG, in a dose-dependent manner. These findings suggest that the receptor has been functionally

refolded and is ready for use as a biomaterial for detecting sweet and umami substances.

In chapter 5, the ligand-binding domain of the human sweet taste receptor was used to evaluate sweet taste substances in a practical manner. Tryptophan fluorescence analysis, a relatively simple approach for measuring sweet taste using T1R2 VFT of human sweet receptors, was used to assess the efficacy of sweet taste compounds. The results of the tryptophan assay could show that T1R2 VFT has human-like selective responses to sweet tastants. In particular, the results of tryptophan analysis expressed as relative sweetness could provide a quick and simple way to interpret ligand binding at the receptor level. Although the tested sweetener concentration was below the human threshold, the measured relative sweetness showed a result similar to a human perception, where other sweeteners are perceived as 'more potent' than sucrose. Furthermore, a T1R2 VFT was immobilized on the floating-electrode of a CNT-FET to develop a practical protein-based biosensor for detecting sweet compounds. The device could detect sweet tastants down to a 0.1 fM with high sensitivity and selectivity. The sensor could detect sweet compounds in commercial beverages such as apple juice and chamomile tea. The T1R2 VFT-based CNT-FET has the potential to be a powerful tool for the detection of sweet substances, as well as having a substantial application in the food sector and fundamental investigation.

In chapter 6, the ligand-binding domain of the human umami taste receptor was used to evaluate umami taste substances and their synergistic effects using tryptophan fluorescence assays. The umami taste ligand efficacy analysis using a tryptophan assay could show human-like responses, indicating synergistic effects between umami tastants. Furthermore, a T1R1 VFT was hybridized with floating electrode-based CNT-FET and a combined with a conductive polymer hydrogel. The

receptors fused in the hydrogel-mediated nanostructures had a great affinity with umami substances in the defined FET microenvironment, which enabled a highly sensitive and selective detection of umami substances down to 1 fM. Moreover, the device achieved a wide dynamic range of 10^{-15} ~ 10^{-1} for umami detection, which covers the human taste threshold. Also, the sensor could evaluate umami intensities in fish extract samples. This hydrogel-mediated CNT-FET with T1R1 VFT can be a practical tool for the detection of umami compounds in foods, as well as having a substantial application in the food sector and fundamental investigation.

In chapter 7, photoreceptors were expressed and purified in both *E. coli* and mammalian cells for further analysis and applications. Using the *E. coli* expression system, all four photoreceptors were produced and reconstituted into NDs. The size and morphology of the photoreceptor NDs were confirmed. These photoreceptor NDs can be a useful tool to better understand the physiological and biochemical mechanisms that occur in human visual receptors. Furthermore, it is expected to contribute to the development of technologies to supplement or replace damaged retinas, such as artificial retinas, based on the understanding.

In chapter 8, photoreceptors can be attractive biomaterial for various potential application, because only four types of photoreceptors are required to identify the broad spectrum of visible light in vision. For photoreceptor NDs, not only it can be utilized to target small molecules such as retinal molecules as in the case of many other GPCR NDs but also can recognize the optical properties targeting light. Several optical measurements using Rho and SW NDs revealed exceptional optical characteristics with a refractive index variation greater than 0.18, which is sufficient for optical devices..[109] Additionally, we achieved outstanding light modulation in PDMS waveguide using a considerable refractive-index variation of photoreceptor NDs with photoactivation. The results suggest that photosensitive NDs, which can

exhibit remarkable refractive index modulation capabilities and construct a retina-mimicking platform, are potential resources for all-optical switching and signal processing applications as well as medical applications. Furthermore, using the virus particles expressing photoreceptors, Rho and SW, an *in vitro* model of the eye-to-brain circuit was developed to transmit signals only in response to light of specific wavelengths. Photosensitive spheroids were successfully mass-produced and transported into a neural circuit *in vitro*. Additionally, photospheroids spontaneously developed axons to the outside, and these axons were connected to intact neurons and neurospheroids. Through these connections, signals generated by the photo-stimulation were transmitted from photospheroids to neural network. Based on these results, we suggest that an *in vitro* eye-to-brain model expressing human photoreceptors could provide a potential platform for screening drugs for the treatment of blindness. Furthermore, various types of photospheroids may also be applied to a visual system capable of recognizing input images beyond simple color perception of light.

In this thesis, various approaches were used to engineer and produce human taste receptors and human photoreceptors, as well as various analyses and applications based on them. A ligand binding domain of human sweet and umami taste receptors were produced and combined with conducting nanomaterials to develop a practical and ultrasensitive bioelectronics tongue. These protein-based biosensors can be applied in practical manner due to their mass production of proteins from *E. coli*, high stability and reusability and facile storage of fabricated biosensor. However, some limitations should be addressed to improve the bioelectronics tongue for practical and commercial use. To develop a stable and reproducible biosensor for practical use, the quality of the conducting nanomaterials should be reproducible, and a method to quantitatively immobilize the same amount

of protein should be established.

The photoreceptors were either produced in *E. coli* and mammalian cells, and they were used in a variety of experiments and applications involving photoactivation. Photoactivation of photoreceptors was observed using various analyses in the presence of the 11-*cis*-retinal molecule, which is required for photoreceptor activation. However, the change from 11-*cis*-retinal to all-*trans*-retinal in the response to light is an irreversible response. The photoreceptor in the human body converts all-*trans*-retinal back to 11-*cis*-retinal with the help of a specific enzyme called retinol dehydrogenase. However, the regeneration process does not occur naturally in artificially produced human photoreceptors. Therefore, the regeneration of retinal molecules using an appropriate enzyme should be established for future photoreceptor applications in biomedicine, such as vision restoration.

Bibliography

1 Ashikawa, Y. *et al.* GFP-based evaluation system of recombinant expression through the secretory pathway in insect cells and its application to the extracellular domains of class C GPCRs. *Protein Sci* **20**, 1720-1734, doi:10.1002/pro.707 (2011).

2 Nuemket, N. *et al.* Structural basis for perception of diverse chemical substances by T1r taste receptors. *Nat Commun* **8**, 15530, doi:10.1038/ncomms15530 (2017).

3 Wade, J. H. *et al.* Microfluidic platform for efficient Nanodisc assembly, membrane protein incorporation, and purification. *Lab Chip* **17**, 2951-2959, doi:10.1039/c7lc00601b (2017).

4 Rosenbaum, D. M., Rasmussen, S. G. & Kobilka, B. K. The structure and function of G-protein-coupled receptors. *Nature* **459**, 356-363, doi:10.1038/nature08144 (2009).

5 Cherezov, V. *et al.* High-resolution crystal structure of an engineered human beta2-adrenergic G protein-coupled receptor. *Science* **318**, 1258-1265, doi:10.1126/science.1150577 (2007).

6 Irannejad, R. & von Zastrow, M. GPCR signaling along the endocytic pathway. *Curr Opin Cell Biol* **27**, 109-116, doi:10.1016/j.ceb.2013.10.003 (2014).

7 Attwood, T. K. & Findlay, J. B. Fingerprinting G-protein-coupled receptors. *Protein Eng* **7**, 195-203, doi:10.1093/protein/7.2.195 (1994).

8 Fredriksson, R., Lagerstrom, M. C., Lundin, L. G. & Schioth, H. B. The G-protein-coupled receptors in the human genome form five main families. Phylogenetic analysis, paralogon groups, and fingerprints. *Mol Pharmacol* **63**, 1256-1272, doi:10.1124/mol.63.6.1256 (2003).

9 Kristiansen, K. Molecular mechanisms of ligand binding, signaling, and regulation within the superfamily of G-protein-coupled receptors: molecular modeling and mutagenesis approaches to receptor structure and function. *Pharmacol Ther* **103**, 21-80, doi:10.1016/j.pharmthera.2004.05.002 (2004).

10 Zhang, R. & Xie, X. Tools for GPCR drug discovery. *Acta Pharmacol Sin* **33**, 372-384, doi:10.1038/aps.2011.173 (2012).

11 Tian, H., Furstenberg, A. & Huber, T. Labeling and Single-Molecule Methods To Monitor G Protein-Coupled Receptor Dynamics. *Chem Rev* **117**, 186-245, doi:10.1021/acs.chemrev.6b00084 (2017).

12 Chun, L., Zhang, W. H. & Liu, J. F. Structure and ligand recognition of class C GPCRs. *Acta Pharmacol Sin* **33**, 312-323, doi:10.1038/aps.2011.186 (2012).

13 Nie, Y., Vigues, S., Hobbs, J. R., Conn, G. L. & Munger, S. D. Distinct contributions of T1R2 and T1R3 taste receptor subunits to the

detection of sweet stimuli. *Curr Biol* **15**, 1948-1952, doi:10.1016/j.cub.2005.09.037 (2005).

14 Jiang, P. *et al.* The cysteine-rich region of T1R3 determines responses to intensely sweet proteins. *J Biol Chem* **279**, 45068-45075, doi:10.1074/jbc.M406779200 (2004).

15 Jiang, P. *et al.* Lactisole interacts with the transmembrane domains of human T1R3 to inhibit sweet taste. *J Biol Chem* **280**, 15238-15246, doi:10.1074/jbc.M414287200 (2005).

16 Allen, S. J., Crown, S. E. & Handel, T. M. Chemokine: receptor structure, interactions, and antagonism. *Annu Rev Immunol* **25**, 787-820, doi:10.1146/annurev.immunol.24.021605.090529 (2007).

17 Xu, H. *et al.* Different functional roles of T1R subunits in the heteromeric taste receptors. *Proc Natl Acad Sci U S A* **101**, 14258-14263, doi:10.1073/pnas.0404384101 (2004).

18 Jiang, P. *et al.* Identification of the cyclamate interaction site within the transmembrane domain of the human sweet taste receptor subunit T1R3. *J Biol Chem* **280**, 34296-34305, doi:10.1074/jbc.M505255200 (2005).

19 Tonosaki, K. & Funakoshi, M. Cyclic nucleotides may mediate taste transduction. *Nature* **331**, 354-356, doi:10.1038/331354a0 (1988).

20 Uchida, Y. & Sato, T. Changes in outward K+ currents in response to two types of sweeteners in sweet taste transduction of gerbil taste cells. *Chem Senses* **22**, 163-169, doi:10.1093/chemse/22.2.163 (1997).

21 Avenet, P., Hofmann, F. & Lindemann, B. Signalling in taste receptor cells: cAMP-dependent protein kinase causes depolarization by closure of 44 pS K-channels. *Comp Biochem Physiol A Comp Physiol* **90**, 681-685, doi:10.1016/0300-9629(88)90684-6 (1988).

22 Margolskee, R. F. Molecular mechanisms of bitter and sweet taste transduction. *J Biol Chem* **277**, 1-4, doi:10.1074/jbc.R100054200 (2002).

23 Zhao, G. Q. *et al.* The receptors for mammalian sweet and umami taste. *Cell* **115**, 255-266, doi:10.1016/s0092-8674(03)00844-4 (2003).

24 Kinnamon, S. C. Umami taste transduction mechanisms. *Am J Clin Nutr* **90**, 753S-755S, doi:10.3945/ajcn.2009.27462K (2009).

25 Fu, Y. in *Webvision: The Organization of the Retina and Visual System* (eds H. Kolb, E. Fernandez, & R. Nelson) (1995).

26 Chabre, M. Trigger and amplification mechanisms in visual phototransduction. *Annu Rev Biophys Biophys Chem* **14**, 331-360, doi:10.1146/annurev.bb.14.060185.001555 (1985).

27 Baneyx, F. & Mujacic, M. Recombinant protein folding and misfolding in Escherichia coli. *Nat Biotechnol* **22**, 1399-1408, doi:10.1038/nbt1029 (2004).

28 Sarramegna, V., Talmont, F., Demange, P. & Milon, A. Heterologous expression of G-protein-coupled receptors: comparison of expression systems from the standpoint of large-scale production and

purification. *Cell Mol Life Sci* **60**, 1529-1546, doi:10.1007/s00018-003-3168-7 (2003).
29 Loll, P. J. Membrane protein structural biology: the high throughput challenge. *J Struct Biol* **142**, 144-153, doi:10.1016/s1047-8477(03)00045-5 (2003).
30 Grisshammer, R. & Tate, C. G. Overexpression of integral membrane proteins for structural studies. *Q Rev Biophys* **28**, 315-422, doi:10.1017/s0033583500003504 (1995).
31 Michalke, K. *et al.* Mammalian G-protein-coupled receptor expression in Escherichia coli: I. High-throughput large-scale production as inclusion bodies. *Anal Biochem* **386**, 147-155, doi:10.1016/j.ab.2008.12.016 (2009).
32 Michalke, K. *et al.* Mammalian G protein-coupled receptor expression in Escherichia coli: II. Refolding and biophysical characterization of mouse cannabinoid receptor 1 and human parathyroid hormone receptor 1. *Anal Biochem* **401**, 74-80, doi:10.1016/j.ab.2010.02.017 (2010).
33 Bane, S. E., Velasquez, J. E. & Robinson, A. S. Expression and purification of milligram levels of inactive G-protein coupled receptors in E. coli. *Protein Expr Purif* **52**, 348-355, doi:10.1016/j.pep.2006.10.017 (2007).
34 Fukuda, N., Kaishima, M., Ishii, J. & Honda, S. Positive Detection of GPCR Antagonists Using a System for Inverted Expression of a Fluorescent Reporter Gene. *ACS Synth Biol* **6**, 1554-1562, doi:10.1021/acssynbio.7b00056 (2017).
35 Schutz, M. *et al.* Directed evolution of G protein-coupled receptors in yeast for higher functional production in eukaryotic expression hosts. *Sci Rep* **6**, 21508, doi:10.1038/srep21508 (2016).
36 Cevheroglu, O., Becker, J. M. & Son, C. D. GPCR-Galpha protein precoupling: Interaction between Ste2p, a yeast GPCR, and Gpa1p, its Galpha protein, is formed before ligand binding via the Ste2p C-terminal domain and the Gpa1p N-terminal domain. *Biochim Biophys Acta Biomembr* **1859**, 2435-2446, doi:10.1016/j.bbamem.2017.09.022 (2017).
37 Glass, M. & Northup, J. K. Agonist selective regulation of G proteins by cannabinoid CB(1) and CB(2) receptors. *Mol Pharmacol* **56**, 1362-1369, doi:10.1124/mol.56.6.1362 (1999).
38 Hartman, J. L. t. & Northup, J. K. Functional reconstitution in situ of 5-hydroxytryptamine2c (5HT2c) receptors with alphaq and inverse agonism of 5HT2c receptor antagonists. *J Biol Chem* **271**, 22591-22597, doi:10.1074/jbc.271.37.22591 (1996).
39 Doi, T. *et al.* Characterization of human endothelin B receptor and mutant receptors expressed in insect cells. *Eur J Biochem* **248**, 139-148, doi:10.1111/j.1432-1033.1997.00139.x (1997).
40 Yang, H. *et al.* Nanodisc-Based Bioelectronic Nose Using Olfactory Receptor Produced in Escherichia coli for the Assessment of the

Death-Associated Odor Cadaverine. *ACS Nano* **11**, 11847-11855, doi:10.1021/acsnano.7b04992 (2017).
41 Lee, M. *et al.* Human-like smelling of a rose scent using an olfactory receptor nanodisc-based bioelectronic nose. *Scientific Reports* **8**, doi:ARTN 13945
10.1038/s41598-018-32155-1 (2018).
42 Kim, K. H. *et al.* Wireless portable bioelectronic nose device for multiplex monitoring toward food freshness/spoilage. *Biosens Bioelectron* **215**, 114551, doi:10.1016/j.bios.2022.114551 (2022).
43 Denisov, I. G. & Sligar, S. G. Nanodiscs in Membrane Biochemistry and Biophysics. *Chem Rev* **117**, 4669-4713, doi:10.1021/acs.chemrev.6b00690 (2017).
44 Kwon, O. S., Song, H. S., Park, T. H. & Jang, J. Conducting Nanomaterial Sensor Using Natural Receptors. *Chem Rev* **119**, 36-93, doi:10.1021/acs.chemrev.8b00159 (2019).
45 Song, H. S. *et al.* Bioelectronic Tongue Using Heterodimeric Human Taste Receptor for the Discrimination of Sweeteners with Human-like Performance. *ACS Nano* **8**, 9781-9789, doi:10.1021/nn502926x (2014).
46 Ahn, S. R. *et al.* Duplex Bioelectronic Tongue for Sensing Umami and Sweet Tastes Based on Human Taste Receptor Nanovesicles. *ACS Nano* **10**, 7287-7296, doi:10.1021/acsnano.6b02547 (2016).
47 Toda, Y. *et al.* Two distinct determinants of ligand specificity in T1R1/T1R3 (the umami taste receptor). *J Biol Chem* **288**, 36863-36877, doi:10.1074/jbc.M113.494443 (2013).
48 Akbar, S. M., Sreeramulu, K. & Sharma, H. C. Tryptophan fluorescence quenching as a binding assay to monitor protein conformation changes in the membrane of intact mitochondria. *J Bioenerg Biomembr* **48**, 241-247, doi:10.1007/s10863-016-9653-0 (2016).
49 Belloir, C. *et al.* Biophysical and functional characterization of the N-terminal domain of the cat T1R1 umami taste receptor expressed in Escherichia coli. *PLoS One* **12**, e0187051, doi:10.1371/journal.pone.0187051 (2017).
50 Ramirez, I. Why do sugars taste good? *Neurosci Biobehav Rev* **14**, 125-134, doi:10.1016/s0149-7634(05)80213-1 (1990).
51 Beauchamp, G. K. Why do we like sweet taste: A bitter tale? *Physiol Behav* **164**, 432-437, doi:10.1016/j.physbeh.2016.05.007 (2016).
52 Ludwig, D. S. The glycemic index: physiological mechanisms relating to obesity, diabetes, and cardiovascular disease. *JAMA* **287**, 2414-2423, doi:10.1001/jama.287.18.2414 (2002).
53 Mann, J. Dietary carbohydrate: relationship to cardiovascular disease and disorders of carbohydrate metabolism. *Eur J Clin Nutr* **61 Suppl 1**, S100-111, doi:10.1038/sj.ejcn.1602940 (2007).
54 Mozaffarian, D. Dietary and Policy Priorities for Cardiovascular Disease, Diabetes, and Obesity: A Comprehensive Review. *Circulation*

133, 187-225, doi:10.1161/CIRCULATIONAHA.115.018585 (2016).
55 Trumbo, P. R. *et al.* Perspective: Measuring Sweetness in Foods, Beverages, and Diets: Toward Understanding the Role of Sweetness in Health. *Adv Nutr* **12**, 343-354, doi:10.1093/advances/nmaa151 (2021).
56 D'Arcy-Moskwa, E., Weston, L., Noble, G. N. & Raidal, S. L. Determination of sucrose in equine serum using liquid chromatography-mass spectrometry (LC/MS). *J Chromatogr B Analyt Technol Biomed Life Sci* **879**, 3668-3671, doi:10.1016/j.jchromb.2011.09.049 (2011).
57 Terol, A., Paredes, E., Maestre, S. E., Prats, S. & Todoli, J. L. Rapid and sensitive determination of carbohydrates in foods using high temperature liquid chromatography with evaporative light scattering detection. *J Sep Sci* **35**, 929-936, doi:10.1002/jssc.201101072 (2012).
58 Habara, M., Ikezaki, H. & Toko, K. Study of sweet taste evaluation using taste sensor with lipid/polymer membranes. *Biosens Bioelectron* **19**, 1559-1563, doi:10.1016/j.bios.2003.06.002 (2004).
59 Shekarchizadeh, H., Ensafi, A. A. & Kadivar, M. Selective determination of sucrose based on electropolymerized molecularly imprinted polymer modified multiwall carbon nanotubes/glassy carbon electrode. *Mater Sci Eng C Mater Biol Appl* **33**, 3553-3561, doi:10.1016/j.msec.2013.04.052 (2013).
60 Ahn, J. H. *et al.* Fiber-optic waveguide coupled surface plasmon resonance sensor. *Opt Express* **20**, 21729-21738, doi:10.1364/OE.20.021729 (2012).
61 Zhang, N. L., Wei, X., Fan, Y. X., Zhou, X. R. & Liu, Y. Recent advances in development of biosensors for taste-related analyses. *Trac-Trend Anal Chem* **129**, doi:ARTN 115925
10.1016/j.trac.2020.115925 (2020).
62 Ahn, S. R. *et al.* High-performance bioelectronic tongue using ligand binding domain T1R1 VFT for umami taste detection. *Biosens Bioelectron* **117**, 628-636, doi:10.1016/j.bios.2018.06.028 (2018).
63 Kim, T. H. *et al.* "Bioelectronic super-taster" device based on taste receptor-carbon nanotube hybrid structures. *Lab Chip* **11**, 2262-2267, doi:10.1039/c0lc00648c (2011).
64 Song, H. S. *et al.* Human taste receptor-functionalized field effect transistor as a human-like nanobioelectronic tongue. *Nano Lett* **13**, 172-178, doi:10.1021/nl3038147 (2013).
65 Wasilewski, T., Kamysz, W. & Gebicki, J. Bioelectronic tongue: Current status and perspectives. *Biosens Bioelectron* **150**, 111923, doi:10.1016/j.bios.2019.111923 (2020).
66 Wee, M., Tan, V. & Forde, C. A Comparison of Psychophysical Dose-Response Behaviour across 16 Sweeteners. *Nutrients* **10**, doi:10.3390/nu10111632 (2018).
67 Fujimaru, T., Park, J. H. & Lim, J. Sensory characteristics and relative sweetness of tagatose and other sweeteners. *J Food Sci* **77**, S323-

328, doi:10.1111/j.1750-3841.2012.02844.x (2012).
68 Nango, E. *et al.* Taste substance binding elicits conformational change of taste receptor T1r heterodimer extracellular domains. *Sci Rep* **6**, 25745, doi:10.1038/srep25745 (2016).
69 Bagal-Kestwal, D., Kestwal, R. M. & Chiang, B. H. Invertase-nanogold clusters decorated plant membranes for fluorescence-based sucrose sensor. *J Nanobiotechnology* **13**, 30, doi:10.1186/s12951-015-0089-1 (2015).
70 Yeh, P. H., Li, Z. & Wang, Z. L. Schottky-Gated Probe-Free ZnO Nanowire Biosensor. *Adv Mater* **21**, 4975-4978, doi:10.1002/adma.200902172 (2009).
71 Heller, I. *et al.* Identifying the mechanism of biosensing with carbon nanotube transistors. *Nano Lett* **8**, 591-595, doi:10.1021/nl072996i (2008).
72 Li, X. *et al.* Human receptors for sweet and umami taste. *Proc Natl Acad Sci U S A* **99**, 4692-4696, doi:10.1073/pnas.072090199 (2002).
73 Zhang, F. *et al.* Molecular mechanism of the sweet taste enhancers. *Proc Natl Acad Sci U S A* **107**, 4752-4757, doi:10.1073/pnas.0911660107 (2010).
74 Masuda, K. *et al.* Characterization of the modes of binding between human sweet taste receptor and low-molecular-weight sweet compounds. *PLoS One* **7**, e35380, doi:10.1371/journal.pone.0035380 (2012).
75 Hunter, S. R., Reister, E. J., Cheon, E. & Mattes, R. D. Low Calorie Sweeteners Differ in Their Physiological Effects in Humans. *Nutrients* **11**, doi:10.3390/nu11112717 (2019).
76 Bernhardt, S. J., Naim, M., Zehavi, U. & Lindemann, B. Changes in IP3 and cytosolic Ca2+ in response to sugars and non-sugar sweeteners in transduction of sweet taste in the rat. *J Physiol* **490 (Pt 2)**, 325-336, doi:10.1113/jphysiol.1996.sp021147 (1996).
77 Servant, G., Tachdjian, C., Li, X. & Karanewsky, D. S. The sweet taste of true synergy: positive allosteric modulation of the human sweet taste receptor. *Trends Pharmacol Sci* **32**, 631-636, doi:10.1016/j.tips.2011.06.007 (2011).
78 Fernstrom, J. D. *et al.* Mechanisms for sweetness. *J Nutr* **142**, 1134S-1141S, doi:10.3945/jn.111.149567 (2012).
79 Ma, X., Zhao, D., Li, X. & Meng, L. Chromatographic method for determination of the free amino acid content of chamomile flowers. *Pharmacogn Mag* **11**, 176-179, doi:10.4103/0973-1296.149735 (2015).
80 Zhang, L., Cao, Q. Q., Granato, D., Xu, Y. Q. & Ho, C. T. Association between chemistry and taste of tea: A review. *Trends Food Sci Tech* **101**, 139-149, doi:10.1016/j.tifs.2020.05.015 (2020).
81 Wu, B. *et al.* Mechanisms of umami taste perception: From molecular level to brain imaging. *Crit Rev Food Sci Nutr* **62**, 7015-7024, doi:10.1080/10408398.2021.1909532 (2022).

82 Andres-Hernando, A. *et al.* Umami-induced obesity and metabolic syndrome is mediated by nucleotide degradation and uric acid generation. *Nat Metab* **3**, 1189-1201, doi:10.1038/s42255-021-00454-z (2021).
83 Liu, J. *et al.* A novel umami electrochemical biosensor based on AuNPs@ZIF-8/Ti3C2 MXene immobilized T1R1-VFT. *Food Chem* **397**, 133838, doi:10.1016/j.foodchem.2022.133838 (2022).
84 Son, M. & Park, T. H. The bioelectronic nose and tongue using olfactory and taste receptors: Analytical tools for food quality and safety assessment. *Biotechnol Adv* **36**, 371-379, doi:10.1016/j.biotechadv.2017.12.017 (2018).
85 Li, M. *et al.* Biomimetic ion nanochannels for sensing umami substances. *Biomaterials* **282**, 121418, doi:10.1016/j.biomaterials.2022.121418 (2022).
86 Karami, P. *et al.* Composite Double-Network Hydrogels To Improve Adhesion on Biological Surfaces. *ACS Appl Mater Interfaces* **10**, 38692-38699, doi:10.1021/acsami.8b10735 (2018).
87 Guan, L., Yan, S., Liu, X., Li, X. & Gao, G. Wearable strain sensors based on casein-driven tough, adhesive and anti-freezing hydrogels for monitoring human-motion. *J Mater Chem B* **7**, 5230-5236, doi:10.1039/c9tb01340g (2019).
88 Darnell, M. C. *et al.* Performance and biocompatibility of extremely tough alginate/polyacrylamide hydrogels. *Biomaterials* **34**, 8042-8048, doi:10.1016/j.biomaterials.2013.06.061 (2013).
89 Mulko, L., Pereyra, J. Y., Rivarola, C. R., Barbero, C. A. & Acevedo, D. F. Improving the retention and reusability of Alpha-amylase by immobilization in nanoporous polyacrylamide-graphene oxide nanocomposites. *Int J Biol Macromol* **122**, 1253-1261, doi:10.1016/j.ijbiomac.2018.09.078 (2019).
90 Zhao, C. *et al.* Probing structure-antifouling activity relationships of polyacrylamides and polyacrylates. *Biomaterials* **34**, 4714-4724, doi:10.1016/j.biomaterials.2013.03.028 (2013).
91 Jeong, J. Y. *et al.* Ultrasensitive Bioelectronic Tongue Based on the Venus Flytrap Domain of a Human Sweet Taste Receptor. *ACS Appl Mater Interfaces* **14**, 2478-2487, doi:10.1021/acsami.1c17349 (2022).
92 Huang, Y. *et al.* Preliminary research on the receptor-ligand recognition mechanism of umami by an hT1R1 biosensor. *Food Funct* **10**, 1280-1287, doi:10.1039/c8fo02522c (2019).
93 Hong, H., Regenstein, J. M. & Luo, Y. The importance of ATP-related compounds for the freshness and flavor of post-mortem fish and shellfish muscle: A review. *Crit Rev Food Sci Nutr* **57**, 1787-1798, doi:10.1080/10408398.2014.1001489 (2017).
94 Skjerdal, T., Reitehaug, E. & Eckner, K. Development of performance objectives for Listeria monocytogenes contaminated salmon (Salmo salar) intended used as sushi and sashimi based on analyses of naturally contaminated samples. *Int J Food Microbiol* **184**, 8-13,

doi:10.1016/j.ijfoodmicro.2014.03.031 (2014).
95 Kulawik, P. & Kumar Tiwari, B. Recent advancements in the application of non-thermal plasma technology for the seafood industry. *Crit Rev Food Sci Nutr* **59**, 3199-3210, doi:10.1080/10408398.2018.1510827 (2019).
96 Dawei Yu, D. J., Fang Yang, Pei Gao, Qixing Jiang, Yanshun Xu, Peipei Yu, Wenshui Xia. The factors influencing the flavor characteristics of frozen obscure
pufferfish (Takifugu Obscurus) during storage: Ice crystals, endogenous
proteolysis and oxidation. *International Journal of Refrigeratio* **122**, 147-155 (2021).
97 Kadiyala, P. *et al.* High-Density Lipoprotein-Mimicking Nanodiscs for Chemo-immunotherapy against Glioblastoma Multiforme. *ACS Nano* **13**, 1365-1384, doi:10.1021/acsnano.8b06842 (2019).
98 Jiang, M. S., Xu, X. L., Yang, T., Zhang, X. D. & Li, F. Refractive index redistribution with accommodation based on finite volume-constant age-dependent mechanical modeling. *Vision Res* **160**, 52-59, doi:10.1016/j.visres.2019.04.008 (2019).
99 Nemoto, S. Measurement of the refractive index of liquid using laser beam displacement. *Appl Opt* **31**, 6690-6694, doi:10.1364/AO.31.006690 (1992).
100 Meadway, A. & Sincich, L. C. Light reflectivity and interference in cone photoreceptors. *Biomed Opt Express* **10**, 6531-6554, doi:10.1364/BOE.10.006531 (2019).
101 Park, B. *et al.* Artificial Rod and Cone Photoreceptors with Human-Like Spectral Sensitivities. *Adv Mater* **30**, e1706764, doi:10.1002/adma.201706764 (2018).
102 Amer, M. S., Wang, W., Kollins, K., Altalebi, H. & Schwingenschlogl, U. On the evaporation kinetics of [60] fullerene in aromatic organic solvents. *Phys Chem Chem Phys* **20**, 11296-11305, doi:10.1039/c8cp01076e (2018).
103 Kim, J. H., Kwak, B. K., Ha, M., Cheong, H. K. & Yi, J. Modeling human exposure levels to airborne volatile organic compounds by the hebei spirit oil spill. *Environ Health Toxicol* **27**, e2012008, doi:10.5620/eht.2012.27.e2012008 (2012).
104 Knierim, B., Hofmann, K. P., Gartner, W., Hubbell, W. L. & Ernst, O. P. Rhodopsin and 9-demethyl-retinal analog: effect of a partial agonist on displacement of transmembrane helix 6 in class A G protein-coupled receptors. *J Biol Chem* **283**, 4967-4974, doi:10.1074/jbc.M703059200 (2008).
105 Tsukamoto, H. & Terakita, A. Diversity and functional properties of bistable pigments. *Photochem Photobiol Sci* **9**, 1435-1443, doi:10.1039/c0pp00168f (2010).
106 Bandara, S. *et al.* Photoactivation mechanism of a carotenoid-based photoreceptor. *Proc Natl Acad Sci U S A* **114**, 6286-6291, doi:10.1073/pnas.1700956114 (2017).

107 Wu, D. M. *et al.* Chemically Responsive Elastomers Exhibiting Unity-Order Refractive Index Modulation. *Adv Mater* **30**, doi:10.1002/adma.201703912 (2018).
108 Valouch, S. *et al.* Direct fabrication of PDMS waveguides via low-cost DUV irradiation for optical sensing. *Opt Express* **20**, 28855-28861, doi:10.1364/OE.20.028855 (2012).
109 Taylor, H. F. Optical switching and modulation in parallel dielectric waveguides. *J. Appl. Phys.* **44 (7)**, 3257–3262 (1973).

국문초록

G 단백질 결합 수용체(GPCR)는 가장 큰 부류의 막횡단 단백질 패밀리로 시각, 미각, 후각, 신경전달물질 및 호르몬과 같은 대부분의 세포 반응을 매개한다. GPCR의 활동과 기능을 측정하는 것은 식품, 환경 및 생물의학 응용 분야에서 매우 중요하다. 따라서 기능적인 GPCR을 생산하고 공정하는 것은 GPCR 연구 및 실제 응용을 위한 도구를 개발하는 데 중요하다. 인간에게는 시각, 미각, 후각, 청각, 촉각의 다섯 가지 감각이 있다. 오감 중 시각, 미각, 후각은 GPCR 신호전달을 포함한다. A 클래스 GPCR에는 시각과 후각을 담당하는 광수용체와 후각 수용체가 포함된다. 클래스 C GPCR에는 종종 "맛있는" 맛으로 알려진 단맛과 감칠맛에 대한 미각 수용체가 포함된다.

본 연구에서는 다양한 접근 방식을 수행하여 인간의 미각 수용체와 시각 광수용체를 생산하였다. 인간의 단맛 및 감칠맛 수용체를 활용하기 위해 대장균에서 과발현하기 어려운 전체 수용체를 사용하는 대안으로 수용체의 주요 리간드 결합 도메인을 대장균으로부터 대량생산하였다. 생산된 T1R2 VFT와 T1R1 VFT는 실용적인 방식으로 단맛과 감칠맛을 평가하기 위해 트립토판 형광 분석으로 독립적으로 분석되었고 전도성 나노 물질과 결합하여 단맛 및 감칠맛 센서를 제작하였다. 대장균에서 생산한 인간 광수용체 나노디스크와 동물세포에서 생산한 광수용체 발현 바이러스는 여러 분석과 응용을 통해 인간 광수용체의 생리학적 및 생화학적 메커니즘을 더 잘 이해하고 이를 통한 시각 복원 기술 개발에 적용하고자 하였다.

첫째, 인간의 단맛 및 감칠맛 수용체의 주요 리간드 결합 도메인인 T1R2 VFT 및 T1R1 VFT는 전체 수용체를 사용하는 대안 전략으로 대장균에서 기능적으로 생성하였다. VFT의 기능은 각각 대표적인 맛 물질인 수크로스와 MSG를 사용하여 트립토판 형광 분석을 사용하여 테스트하였다. 기능적으로 생산된 VFT는 단맛과 감칠맛 물질을 감지하기 위한 생체 재료로 사용하기 위해 분석 및 검증하였다.

둘째, 인간의 단맛 수용체의 주요 리간드 결합 도메인을 이용하여 실질적인 단맛 물질을 평가하였다. 인간 단맛 수용체의 T1R2 VFT를 사용하여 단맛을 측정하는 비교적 간단한 접근법인 트립토판 형광 분석을 사용하여 단맛 물질에 대한 효능을 평가하였다. 트립토판 분석 결과는 수용체 수준에서 리간드 결합을 해석하는 빠르고 간단한 방법을 제공하기 위해 수크로스에 대한 상대적인 단맛으로 표현되었다. 또한, T1R2 VFT를 CNT-FET의 전극에 고정화하여 단맛을 감지하는 실용적인 단백질 기반 바이오 센서를 제작하였다.

셋째, 인간 감칠맛 수용체의 주요 리간드 결합 도메인을 사용하여 감칠맛 물질과 물질간의 시너지 효과를 트립토판 형광 분석을 통해 평가하였다. 또한, T1R1 VFT는 플로팅 전극 기반 CNT-FET에 고정하였고 전도성 고분자 하이드로겔과 결합하였다. T1R1 VFT를 포함하는 하이드로겔 매개 CNT-FET는 식품에서 감칠맛 화합물을 검출하는 데 유용한 도구일 뿐만 아니라 식품 부문 및 기초 연구에서 중요한 응용을 가질 것으로 예상된다.

마지막으로 광수용체는 대장균과 동물 세포에서 생산하여 다양한 실험과 응용에 사용하였다. 대장균에서 생산된 광수용체 나노디스크는 광

학 스위칭과 같은 잠재적인 광학 응용 분야에 사용하기 위한 특성을 측정하는 데 사용하였다. 동물세포에서 생산된 광수용체 발현 바이러스는 눈에서 뇌로 가는 신경 회로의 시험관 내 모델 개발에 사용하였다.

본 연구에서는 인간의 미각 수용체와 시각 광수용체를 생산하고 공정하는 다양한 접근 방식을 적용하였다. 인간의 미각과 시각에 대한 더 나은 이해와 미래의 식품, 환경 및 생물 의학 응용을 위해 인공적으로 생산한 인간 감각 수용체를 사용한 다양한 분석 및 응용도 조사하였다.

주요어: 인간 단맛 수용체, 인간 감칠맛 수용체, 인간 광수용체, 리간드 결합 도메인, 나노바이오센서, 나노디스크

학 번: 2017-29229